UiO : University of Oslo

Reyna Guadalupe Ramírez de la Torre

Experiments on Bubble and Droplet Production in Falling Jets and Breaking Waves

Thesis submitted for the degree of Philosophiae Doctor

Department of Mathematics
Faculty of Natural Sciences and Mathematics

2021

Series of dissertations submitted to the
Faculty of Mathematics and Natural Sciences, University of Oslo
No. 2386

ISSN 1501-7710

Cover: Hanne Baadsgaard Utigard.
Print production: Reprosentralen, University of Oslo.

Preface

This thesis is submitted in partial fulfillment of the requirements for the degree of *Philosophiae Doctor* at the University of Oslo. The research presented here was conducted at the University of Oslo, under the supervision of professor Atle Jensen, professor Geir K. Pedersen and Dr. Miroslav Kuchta. The experiments were carried out in the Hydrodynamics Laboratory at UiO. Additional cameras for the 3DPTV setup was partially funded by RCN project "RigSpray", grant number 256435.

The thesis is a collection of three papers and one report, presented in chronological order of writing. The common theme is the implementation of Particle Tracking Velocimetry, and in particular, three-dimensional Particle Tracking Velocimetry as a new technique in the Hydrodynamics Laboratory. The papers are preceded by an introductory chapter that relates them to each other and provides background information and motivation for the work. I am the first author in all papers, and carried out most of the experimental work and research done. The only exception is the collaboration with Dr. Petter Vollestad in the second paper, where he carried out the experiments related to the air phase measurements and contributed to the writing process.

Reyna Guadalupe Ramírez de la Torre
Oslo, March 2021

Acknowledgements

First I would like to acknowledge all my coauthors, they are also the closest working group I have and the reason why I was able to land ideas and get results. So thanks to Atle, Geir, Miro and Petter for all your help, ideas and discussions. Without them this work would not be possible. In the same order, I would like to acknowledge the help of Olav, our lab engineer. The long hours put into developing the experimental set-ups and tools, even when they seem a bit crazy, are something I really appreciate. And again, without them this work would not be possible.

I would like to thank the colleagues in the Mechanics Section for the nice times spent during lunches, meetings and long days of lab work. Especially those ones that help me or together with me understood the difficulties of a new country, new position, new everything... Thanks to Rossana, Yiyi, Lisa, Sussane, Christian, Tak and Blandine.

I would also like to acknowledge the help and support of my family: my parents, Reyna and Juan José, and my brothers, César and Pepe. Their understanding and help when being so far away have kept me afloat and moving forward. Even with the difficult times that the year 2020 brought, their advice, love and aid were a light illuminating the pad through the dark times. Thank you is just not enough.

Last but not least, I would like to thank the help and support of Henrik. Without you I would not have found this position nor be able to go as far as I have gone. Your input and help as a fellow physicist is as big and important as your love and understanding. Thanks for all these years of good company through the hard times and the nice times.

Reyna Guadalupe Ramírez de la Torre
Oslo, March 2021

"The waves fell; withdrew and fell again,
like the thud of a great beast stamping."
Virginia Woolf, The Waves

Contents

List of Figures

List of Tables

List of Papers

Papers included in this thesis

Paper I

R.G. Ramírez de la Torre, Mirolsav Kuchta and Atle Jensen. "Experiments on air entrainment produced by a circular free falling jet". In: *International Journal of Multiphase Flow.* Vol. 132, 103424, ISSN 0301-9322, DOI: 10.1016/j.ijmultiphaseflow.2020.103424.

Paper II

R.G. Ramírez de la Torre, Mirolsav Kuchta and Atle Jensen. "3D Particle Tracking Velocimetry applied to bubble plumes from a free falling jet". In: *Proceedings of the 13th International Symposium on Particle Image Velocimetry – ISPIV 2019.*

Paper III

R.G. Ramírez de la Torre, Petter Vollestad and Atle Jensen. "Experimental Investigation of Droplet Distributions from a Plunging Breaker with Different Wind Conditions". Resubmitted to *Journal of Geophysical Research: Oceans.* Available in ESSOAR: DOI: 10.1002/essoar.10504843.1.

Paper IV

R.G. Ramírez de la Torre. "Experiments on Droplet Production from Solitary Waves Impacting on a Vertical Wall". To be submitted.

Relevant paper not included

Paper V

Trygve K. Løken, Thea J. Ellevold, R. G. Ramirez de la Torre, Jean Rabault, Atle Jensen. "Bringing optical fluid motion analysis to the field: a methodology using an open source ROV as camera system and rising bubbles as tracers." In: *Measurement Science and Technology.* Available in http://iopscience.iop.org/article/10.1088/1361-6501/abf09d

Chapter 1

Introduction

The development of research and exploration in Arctic waters is very common nowadays. One of the environmental difficulties in these regions is marine icing. Marine icing is the process of generating thick layers of ice on top of a surface in short periods of time, its consequences has been documented for several years (Ryerson 1990). Marine icing is caused by atmospheric sources and sea spray (Bodaghkhani et al. 2016), but sea spray is considered the main source of icing (Borisenkov and Pchelko 1975). Sea spray is generated by wave collisions, breaking of waves due to strong winds and bursting bubbles that float upon the waves (Lozowski, Szilder, and Makkonen 2000; O'Dowd et al. 2008; Rashid, Khawaja, and Edvardsen 2016).

Figure 1.1: Marine Icing examples. To the left, photography from field measurements in Svalbard (Picture taken by Atle Jensen, 2017). To the right, crew of ship removing icing obtained from Cook and Chatterton 2008.

The ice accretion begins to occur after the generation of sea spray, when the air temperature drops below the freezing point of seawater. The droplets carried by cold air impinge on the structure, creating ice and a liquid water film. The liquid water drains under the gravity but sometimes a small quantity can be entrapped in small pockets. With the growth of ice thickness, sea salt precipitates, creating pure ice (Rashid, Khawaja, and Edvardsen 2016). Heavy ice accretion poses a threat to the stability of ships and offshore structures,for example by shifting their centre of gravity. The understanding of this phenomenon is important

for the safety of installations, ships and people that operates in the cold polar environments.

The multi-scale nature and complexity of spray and icing requires that the research on this field is separated into smaller problems. Some of the smaller problems can be: the modeling of the free-surface; wave slamming; air entrainment during the impact; water sheet and jet formation during the wave slamming; water sheet and droplet breaking caused by wind, and droplet trajectories when they meet the surface on ship or structure (Bodaghkhani et al. 2016; Dommermuth et al. 2007).

In this thesis, the focus of the author was to conduct experiments to bring understanding of the spray phenomena. Size distributions of spray and bubbles are not well known and they are an important input for simulation of waves and splashing of water on structures. The goal was to measure the size distribution and kinematics of the droplets and bubbles produced by waves breaking or splashing on obstacles in the Hydrodynamics Laboratory of the University of Oslo.

The measurement of spray and air entrainment is not an easy task. Different techniques have been used but the characteristics of the phenomena also show each technique limitations. The challenges to overcome are the three-dimensionality, the highly turbulent regions, and the wide distributions for sizes in both droplets and bubbles. For the case of bubble generation in waves and jets, the estimation of the air content and the size distribution has been estimated using: optical probes, conductivity probes, resistivity probes and acoustic probes (Chanson, S. Aoki, and Hoque 2006; Deane 1997; Kolaini 1998; Wang, Bertola, and Chanson 2016). All of these probes are invasive methods with one point measurements. For highly turbulent flows these techniques are non-adequate.

Measuring droplets, and in some cases bubbles, can be done with imaging methods. The use of videos and images with shadowgraphy, or laser sheets are the most common techniques. The post processing of these images can be done by Particle Tracking Velocimetry (PTV). PTV algorithms are used to follow the different particles in their individual trajectories through time (Lagrangian approach). Using more than one camera at the same time allows the reconstruction of the kinematics of the particles in 3D. The advantage of this kind of algorithms is that they consider the camera parameters to estimate the positions of the found particles and correlate the images from the different cameras to reduce the uncertainties on the positions for each particle at each time step. In this thesis, the author decided to use imaging techniques and PTV to analyze different experiments that can be relevant in the understanding of bubble and droplet formation from breaking waves. In the next sections a brief literature review is presented for the relevant topics: Air entrainment and Ocean Spray Production. Then, in the second chapter a detail description of the experimental work is given.

1.1 Air entrainment from a circular jet

During wave breaking, there is a considerable amount of air crossing the water surface and mixing. In general, breaking waves play an important role in the ocean-atmosphere processes by entraining bubbles into the ocean. Therefore, the study of air entrainment is important for understanding these processes. Bubble plumes are generated during the entrainment processes. The bubble plume can appear very dense and consist predominantly of large air cavities that collapse into smaller bubbles and are driven down into the water, reaching a certain maximum depth. Then the bubble clouds spread horizontally and large bubbles and air cavities rise back to the surface to burst (Deike, Melville, and Popinet 2016).

To understand the process of air entrainment on a more fundamental level, studies of plunging jets have been made as prototypes of breaking waves. The analogy between a plunging breaker and a plunging jet might be valid during the first seconds of wave breaking. Several studies have been made to estimate the air entrainment from different jet geometries. The most common ones are the circular jet and planar jet (Chanson, S. Aoki, and Hoque 2006; Chanson 1996; Chanson, S.-i. Aoki, and Maruyama 2002). In this case we will focus only on the circular jet, which has been studied experimental and theoretically. For example, theoretical descriptions of the entrainment process have been made by Kiger and Duncan 2012; McKeogh and Ervine 1981; Zhu, OĞUZ, and Prosperetti 2000. It is generally acknowledged that the air entrainment process is controlled by several parameters. For the circular jet, the geometry of the nozzle will determine the behavior of the liquid flow. The flow instabilities are one of the primary producers of the disturbances. In several experimental studies, once a nozzle geometry is defined, the most commonly used parameter to address the entrainment threshold is the velocity of the jet (Chanson, S. Aoki, and Hoque 2006; Wang, Bertola, and Chanson 2016.)

A thorough compilation of previous results has been made in Kiger and Duncan 2012, where the process before and after the entrainment threshold has been described. The critical condition for air entrainment can occur in different ways (see Figure 1.2). In one case, there are no disturbances on the jet surface; only a meniscus is present which breaks when the steady-state is no longer possible. In the other case, the interface is destabilized by the disturbances within the impinging jet and/or receiving pool causing the meniscus to break. The last case can be further divided into case (i) with small disturbances such that the jet appears smooth and laminar, and case (ii) with disturbances such that the jet appears visibly rough. The type of air entrainment that is observed in the present work is of class (ii). Other criterion to classify the entrainment conditions was to consider when the jet separated into droplets before entering the surface. Biń 1993 summarized the data available for both cases. The main conclusion was that the droplet regime was well correlated to a Weber number power law, but there was no strong or reliable correlation for the continuous jet regime.

During the present investigation, a circular falling jet is used as a first

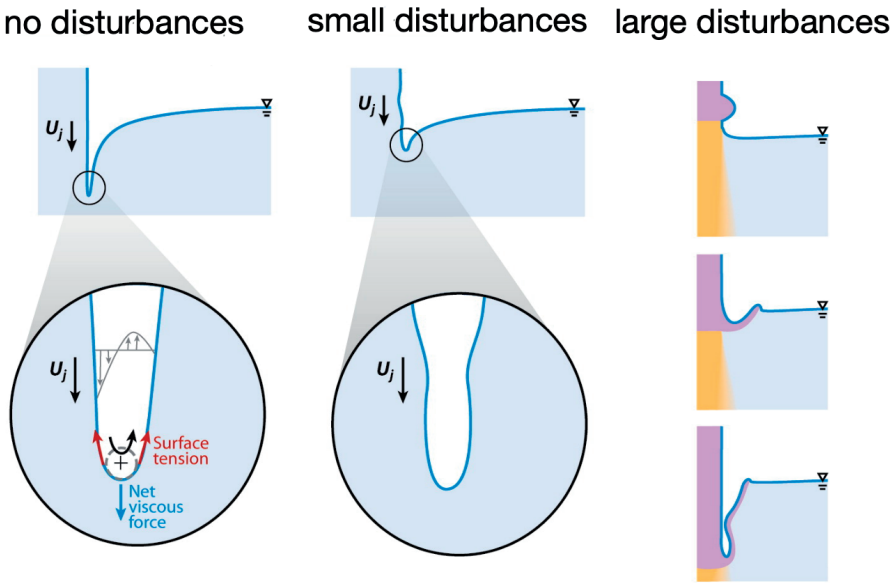

Figure 1.2: Schematic representation of the different air entrainment mechanisms for a circular jet. The bubbles can be created by the following mechanisms: from left to right, a smooth jet (no disturbances), by small disturbances in the surface or by large disturbances. Image modified from Kiger and Duncan 2012.

approach to wave breaking. In the studied case, visible disturbances were developed on the surface of the jet, this disturbances were the main source of air entrainment. The main contribution of this study could be that the conducted experiments were less controlled than previous works and opened a window for a statistical analysis that could potentially be extended to more realistic circumstances outside the laboratory. Although the original plan was to combine the experimental results with simulations, the experimental findings turn out to be very rich and sufficient to create an all-experimental paper, presented in Paper I. While relations between the falling jet and the created bubble plume were made, this first investigation failed on presenting a 3D kinematics of the bubble plume. This was therefore addressed in a new investigation that was presented in the International Symposium of Particle Image Velocimetry, 2019 in Munich, Germany. The correspondent results were published in the Proceedings of the symposium and presented here in Paper II.

1.2 Ocean Spray and Droplet Production

Ocean spray comprises of liquid droplets ejected from the sea surface, generally due to breaking waves and related phenomena. Once ejected from the ocean surface, spray drops are transported and dispersed in the marine atmospheric boundary layer. Marine aerosols span a large range of sizes, from a few nanometers to several millimeters. The smaller particles have residence times in the atmosphere of days to weeks. The larger droplets remain suspended in the

atmosphere from fraction of seconds to several minutes and typically settle back into the ocean if there are no obstacles in the way (Veron 2015).

The formation of marine aerosol is a very complex and broad phenomenon. In this thesis, I only concentrated on a small part of it, that is the formation of droplets from the ocean surface. There are several mechanisms of spray formation. The most studied mechanisms are film, jet and spume droplets (see Figure 1.3). Film and jet droplets are produced when bubbles that were previously entrained in the water, rise to the surface and burst. Spume droplets occur when the wind shear at the surface is sufficiently high to tear off droplets from the surface of waves (Andreas 2002; Andreas et al. 1995). Much less is known about the latter mechanism compared to the bubble bursting generation. Several studies have been made in laboratories. Some of them give an insight on the size distribution of the droplets but the results are relatively wide. In some cases measured drops had a radius up to 700 microns (Fairall et al. 2009), but other studies measured up to 2 mm radius in the laboratory(Veron 2015). Furthermore, field measurements have been conducted, where the concentration of aerosol numbers in the atmospheric boundary layer were obtained (Lenain and Melville 2017). Droplet sizes ranging from 0.1 to 200 microns were considered. It was found that droplets with radii larger than 40 microns can reach heights larger than 400 m above mean sea level.

Figure 1.3: The main mechanisms of sea spray production. Spray can be produced by bursting bubbles (film and jet droplets) or ejected from the crest of breaking waves by the effect of wind (spume droplets). Image modified from Veron 2015.

Another mechanism of droplet formation that has been less studied, is the creation of droplets by wave slamming. When the wave breaks onto the water surface or onto other structures, a large amount of droplets can be created and transported far distances by the wind. In this thesis, the understanding of the droplet formation due to splashes was one of the main focus. The first situation studied was the breaking of a wave onto the water surface, and the variation of the droplet production when wind is included. The results of this investigation

are presented in Paper III.

The next phenomenon of interest is the splash created by a wave impacting solid surfaces. In this case, only field studies from vessels have been made. These studies mainly report the vertical distribution of the Liquid Water Content above the ship bow and do not include information of the velocity of water droplets or their size distribution (Ryerson 1990). In the laboratory, breaking wave impacts on a wall have been studied. Impact pressure, fluid velocity and surface elevation were monitored.

The laboratory studies of wave impact on vertical walls have shown that breaking waves generate the largest pressures and therefore are potentially more dangerous. Several experimental efforts have been made (Bullock et al. 2007; Hattori, Arami, and Yui 1994; Hull and Müller 2002; Jensen 2019; Oumeraci et al. 2001) and mathematical models have been developed to understand the physics behind these processes (Bredmose, Peregrine, and Bullock 2009; Wemmenhove et al. 2015; Wienke and Oumeraci 2005). As result of these efforts, a classification of the impact type has been done and confirmed by several of the mentioned studies. The classification depends primarily on the shape of the wave before the impact and can be summarized in four types (see Figure 1.4):

1. Flip-through. The wave breaks without air entrapment. The formation of an uprising jet in the wall is visible. The pressure can range from “non-breaking" pressure to one single sharp peak.

2. Breaker with small air pocket. The front of the wave is faster than the flip-through and creates a small air pocket when impacting the wall. The pressures have a single sharp peak.

3. Breaker with large air pocket. The front of the wave is fast enough to encapsulate a large air pocket. In these case, after the high peak, the pressure oscillates with high frequency.

4. Turbulent bore. The wave broke previous to the impact generating a turbulent bore. The pressure oscillates with low frequencies.

More recently, a review of the evaluation of impact pressures has been made (Dias and Ghidaglia 2018), where the pressure signals obtained from different wave impacts have been classified using the concept of elementary loading processes (ELP), which was introduced by Lafeber, Bogaert, Brosset, et al. 2012. The review describes wave slamming with the latest numerical and experimental descriptions. The main characteristics of a slamming event are the high force imposed on the solid body with relatively short duration and the quick expansion of the contact region between the liquid jet and the solid body. Any load that a wave impact can induce in a solid body can be described in terms of the ELP’s, which can be classified in three types: ELP1 represents the direct impact; ELP2 represents the building of the jet along the structure, and ELP3 represents the compression of entrapped or escaping gas (see Figure 1.5).

ELP2 is the most common because it appears every time that there is a run up (or down) of the liquid along the object and it is the same ELP presented

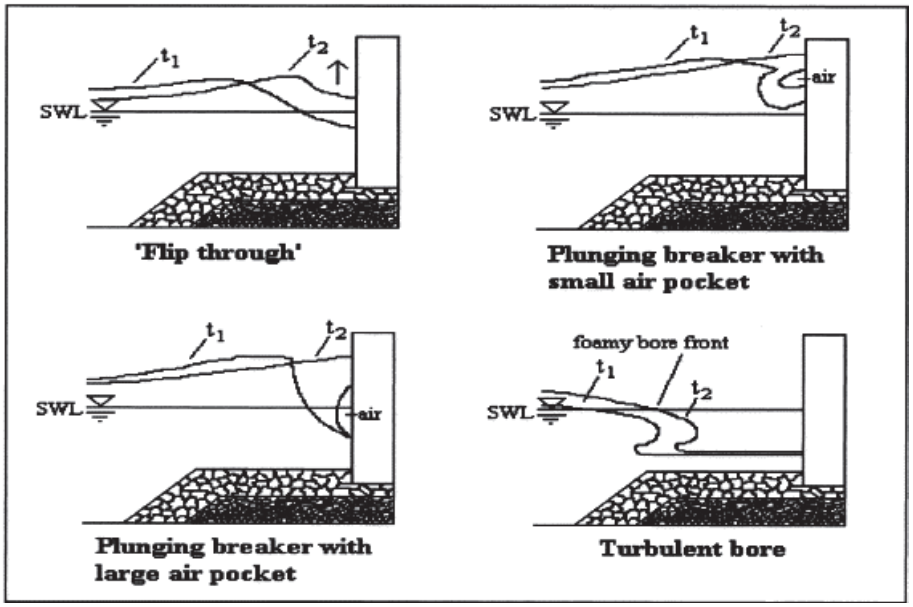

Figure 1.4: Schematic representation of the classification of wave impact depending on the stage of breaking, from Hull and Müller 2002.

in the water entry problem (a body impinging on a liquid pool). Furthermore, ELP2 is the only ELP that can be described by incompressible fluid models and therefore the most studied in the literature. The flip-through impact can be also linked to the ELP2, because very high pressures can be reached when the water level accelerates rapidly along the wall. In contrast, ELP1 and ELP3 have been less studied because of the difficulty to implement compressible fluid models. In the case of ELP3, there is a gas pocket entrapped between the water and the solid body, the gas pocket is compressed by the forward movement of the wave together with the run up at the wall. This gas pocket acts like a spring, where the maximum pressure and frequency of the oscillations depend on the size of the pocket. The direct impact, ELP1, occurs when the liquid particles decelerate rapidly at the contact with the solid. This means a near discontinuity in the velocity that generates a pressure wave inside the liquid and a strain wave inside the solid.

The problem of a liquid impact on a wall has become the primary benchmark for the study of slamming. The global scaling of this problem is well understood but local scaling remains poorly understood (Dias and Ghidaglia 2018). For example, experimental studies in different scales have shown that the shape of the interface does not scale well, the gas-liquid density ratio modifies the shape of the waves before breaking and the instabilities that can appear in the interface are also important in the modification of the interactions of the interface. The variation of the wave front while breaking creates a large range of possibilities both in the magnitude and the shape of the pressure peak (Bogaert et al. 2010; Bullock et al. 2007; Hull and Müller 2002; Meerkerk et al. 2020). Nonetheless, when a solitary wave was studied (Jensen 2019), the plunger breaker with air

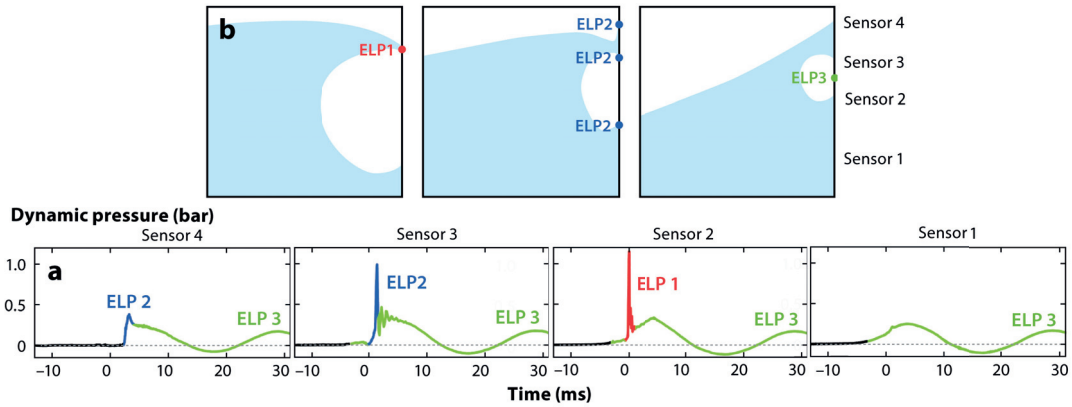

Figure 1.5: Classification of wave impact depending on the ELP, different wave breaking stage will give a different impact pressure signature. Image modified from Dias and Ghidaglia 2018.

pocket produced consistently larger pressure peaks. The pressure profile seems consistent with the wave amplitude and only depends on the breaking stage.

The understanding of the jet formation after the impact and the break up into droplets has been less studied. It is common to consider a simplification of the phenomenon by comparing the wave jet with a planar jet coming out of nozzle (Bodaghkhani et al. 2016; Lozano, Garcıa-Olivares, and Dopazo 1998; Sarchami, Ashgriz, and Tran 2010). As far as the authors know, only Watanabe and Ingram 2015 and Watanabe and Ingram 2016 have conducted experimental work of the break up of waves impacting in a vertical wall and proposed an explanation of the instabilities that generates the spray formation. Also a comparison of the distribution of droplet sizes is made with previous studies. They found that the distribution of sizes in different vertical positions has a lognormal shape and is similar, but not well approximated, by Weibull or Γ-distributions proposed by Roisman, Horvat, and Tropea 2006 and Villermaux, Marmottant, and Duplat 2004, respectively.

The last paper presented in this thesis (Paper IV) presents the results of investigating the droplet formation by a solitary wave impacting on a vertical wall considering different breaking stages. Statistical analysis is made for droplet sizes, velocities and accelerations. And comparison with previous mentioned works is presented.

Over all, there is a large range of parameters and variables that can affect the production of droplets in a breaking wave. It is the aim of this thesis to contribute to the understanding of this complex phenomenon. The author tried to bring a new perspective by using different conditions from the previously studied conditions in other investigations and by using new techniques to acquire the data. In the next chapter, a detailed description of the developed experimental setups and techniques will be done.

Chapter 2

Experimental work

Different experimental techniques were introduced in the Hydrodynamics Laboratory at the University of Oslo during the development of this thesis. The visualization of jet disturbances and the extraction of 3D kinematics by PTV technique were the main contribution of this work. In addition, the usage of 3DPTV to study bubble plumes and spray clouds has not been reported in other studies as far as the author's knowledge goes. In this chapter, the more relevant findings for a successful setup will be summarized. Also, the most common problems to encounter will be presented and analyzed.

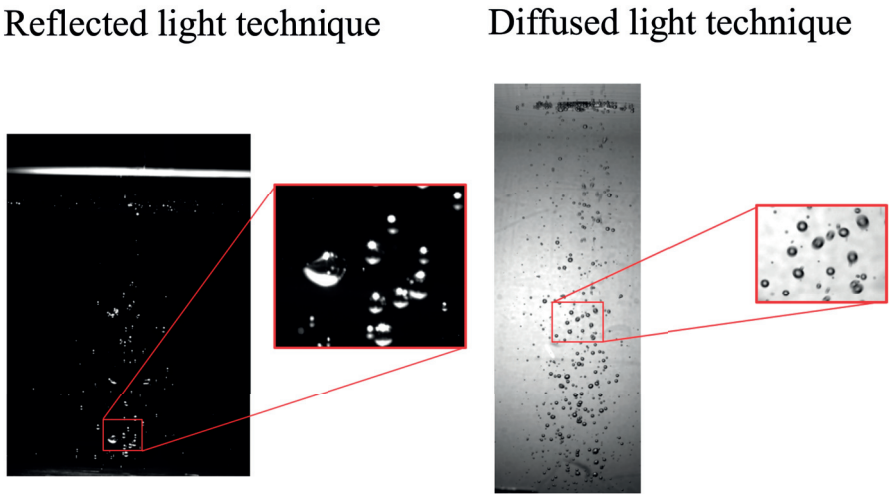

Figure 2.1: The usage of different illumination techniques can have different results, therefore it is important to find the most adequate.

When using fluid tracing techniques, such as PTV, it is common to utilize a dark background and a laser sheet to illuminate the tracer particles. To visualize the bubble plume or droplet cloud, the mentioned technique does not perform well. This technique relies on the reflection of light on the tracers. But when the size of the tracers increases, multiple reflections will appear. Therefore the total amount of particles and the size of the particles cannot be reliably approximated from these reflections. In opposition, if diffused light is used, the shape of the tracers will make a clear dark shadow that will allow us to keep track of the size and position of the different particles. Figure 2.1 shows the difference between both illumination techniques.

For the visualization of the jet, the diffused light illumination technique gives an accurate description of the deformation of the jet surface. As shown in Figure 2.2, the edges of the jet give a clear dark area in the image from where we can extract information of the surface deformation. The same illumination

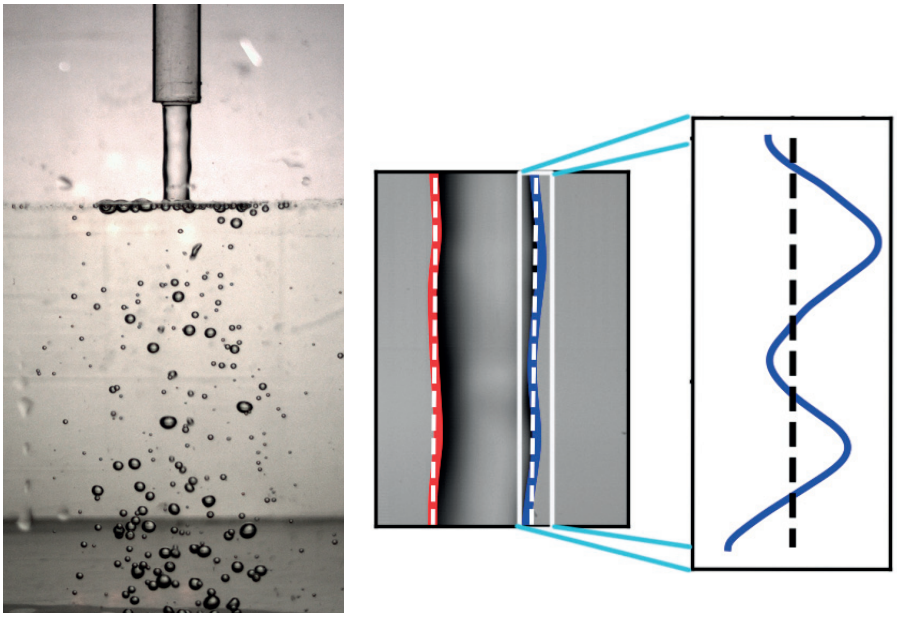

Figure 2.2: To the left, an example picture of the visualization of circular jet ripples creating a bubble plume. To the right, a schematic of the extraction of disturbances from the images.

provides a clear view of the bubbles as mentioned before. Nonetheless, this is opposed to the expected visualization in most PTV algorithms, where it is assumed that the particles will be light on a dark background. In this study we used image processing to invert the gray scale and create images with dark background and light particles from the original diffused light images. This procedure is easily done and does not affect the quality of the images. To achieve this, the gray scale is resampled only by generating the one-to-one function: $F(x) = 256 - x,\ x \in [0, 255]$. As can be seen in the rest of this thesis, the approach gives reliable results without compromising the quality of the data. Although, the use of diffused light images could also be implemented in the algorithms for PTV and then a comparison between the new algorithm results and the results of using image inversion could be made.

2.1 Measuring ripples on a circular jet

The circular jet has been the object of extensive research. At first sight, this phenomenon might seem simple but the research has shown it depends on many parameters that need to be controlled in order to simplify the experiments. In this work we decided to use a statistical approach in order to obtain a setup that goes closer to "real life" phenomena. Although there is a large number of parameters that are left to random effects, the statistical approach helps to obtain relations that can be used in a larger range of similar phenomena and find the link with the proposed theories.

To understand the entrainment produced by a free falling jet, it is important

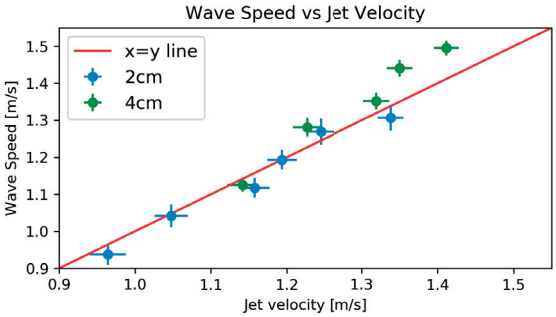

Figure 2.3: Comparison of the median speed of the disturbances displacing down the jet with the estimated velocity of the jet.

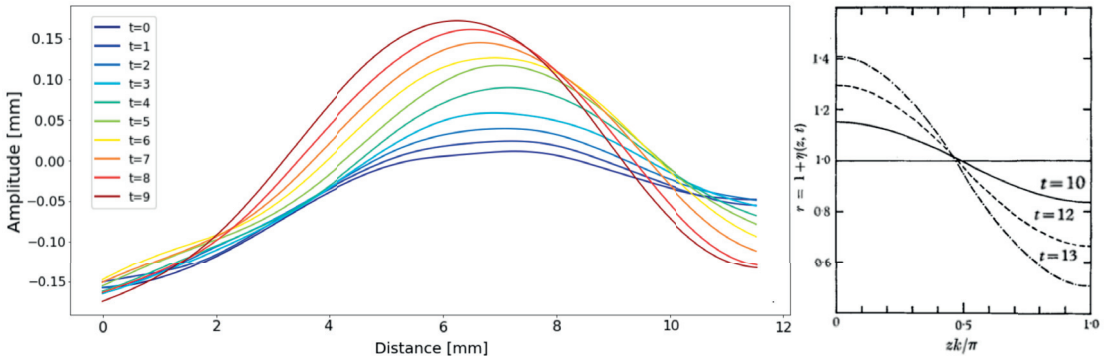

Figure 2.4: Qualitative comparison of the jet disturbances with the theory presented in Yuen 1968.

to understand the deformation of its surface. This deformation has been studied theoretically and experimentally for the last two centuries. Lamb 1932, ch. IX has already summarized the theoretical description of a circular falling jet and the solution for the capillary disturbances presented. It was found that the instabilities of the disturbances on the jet can be related to the steepness, which is the product of the amplitude a and the wave number k. It was also found that while the jet is in downward motion and the motion is steady, the jet exhibits a system of stationary waves, i.e. the formed ripples travel downwards with the velocity of the jet.

To compare this theoretical result with the experiments, the estimated flow velocity was compared with the velocity of the disturbances. The velocity of the disturbances was obtained by a cross-correlation between disturbances in two different time steps. We determine if the compared disturbances are the same disturbance and obtain the spatial displacement between the crest at the different time steps. Then the speed is calculated with the displacement and the time step. Finally, a histogram of the encountered speeds is made and the median speed is considered the speed of the disturbances. The results are compared with the estimated jet velocity in Figure 2.3 for two different jet lengths, only the jets with speeds above 1.4m/s and length of 4cm seems to deviate from the

theory.

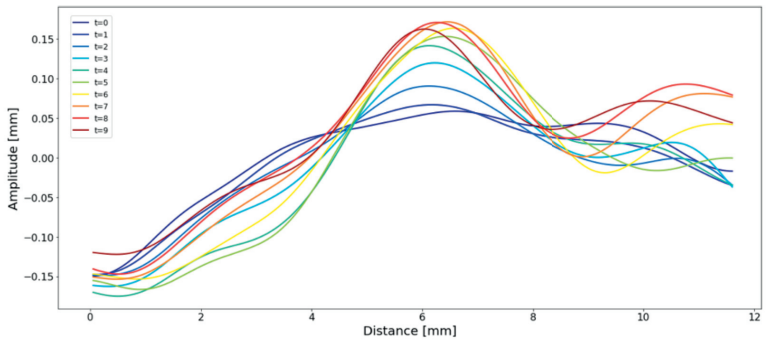

Figure 2.5: An example of the jet disturbances which do not resembles the theory presented in Yuen 1968. Instead of single "wave", we observe the superposition of different wavelengths.

A visualization of the temporal evolution of a single disturbance can be made to compare with the known theory. The theory proposed a third-order model (Yuen 1968) that shows that the asymmetrical development of an initially sinusoidal disturbance in the surface generates higher harmonics and feedback into the fundamental frequency. Figure 2.4 shows a particular case where the evolution of the disturbance has great similarity with the theory. Nonetheless, the shape of the disturbances presented is not always so dreamy. Figure 2.5 shows another case where the followed disturbance has a shape that resembles more to the superposition of several frequencies. The presence of this type of disturbances shows the effects of the uncontrolled jet development and the importance of utilizing a statistical approach.

The conclusions of this study are presented in Paper I. A relation between the characteristics of the jet and the amount of produced bubbles is found. Also, the appendix of that paper studies the effect of the material of the exit tube on the jet disturbances and bubble production. The next step in this investigation of the bubble plume was done by using 3DPTV to visualize the plume. Next section details the difficulties and findings.

2.2 3DPTV setup for bubble plume

The setup used to observe the bubble plume was the same as presented in Paper I, with the difference that 2 cameras were used to obtain the 3D positions of the bubbles, as shown in Figure 2.6. The particle tracking was made with the open source software OpenPTV (OpenPTV et al. 2012) and further post processing was done using Python scripts. As it will be explained in this section, this setup had to be modified in order to obtain the desired results, which are discussed further in Paper II.

The first setup consisted on positioning two cameras at an angle of 90 degrees between each other. In this way, the plane that is not observed by the first camera

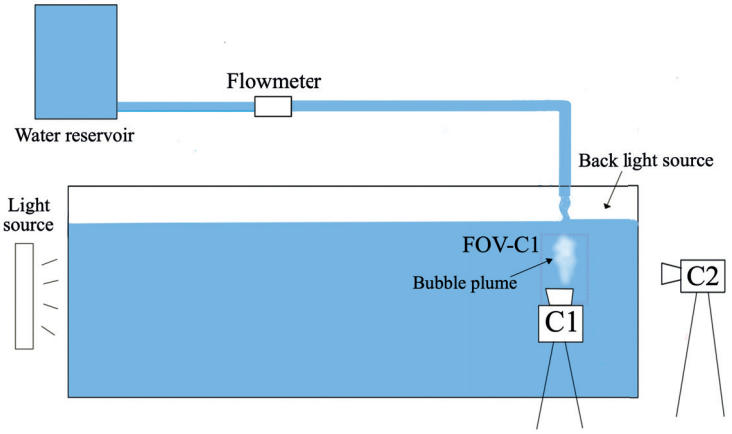

Figure 2.6: Original setup to visualize the bubble plume with only 2 cameras, the cameras are positioned at a 90° angle.

is observed by the other camera. In theory, the position of the bubbles can be found with only 2 cameras for a very sparse plume. Nonetheless, in practice the sparsity of the particles is dependent of size of the field of view and the desired pixel size for the bubbles. To obtain three dimensional trajectories, the particles need to be matched among all views. The method used by OpenPTV finds correspondences based on epipolar geometry (H.-G. Maas 1991a; H.-G. Maas 1991b; H. Maas, Gruen, and Papantoniou 1993) which is roughly described next.

Figure 2.7 depicts the definition of an epipolar line with two cameras. Points $C1$ and $C2$ represent the centers of each camera lens. X_{C1} and X_{C2} are projections of the particle X in the each camera image. The line that joins both lenses centers $\overline{C1C2}$, also has projections in the images, depicted by yellow dots. These dots are known as the epipolar points and together with points X_{C1} and X_{C2} create the correspondent epipolar lines in each image. The epipolar line for X in Camera 2 is shown in red. This epipolar line is only visible in Camera 1 as the point X_{C1}. Then, if more than one bubble sits in the same line $\overline{C_1X}$, all particles X, X_1 and X_2 correspond to the same epipolar line. In which case, only one particle would be seen from Camera 1 and multiple correspondences will arise in Camera 2 $X_{1,C2}$, $X_{2,C2}$ and X_{C2}.

To choose a particle in $C2$ we define a search area, during the calibration. A tolerance width is defined to this epipolar line segment, the search area for the corresponding particle image becomes a narrow two-dimensional bandshaped window in image space. Due to the large number of particles, two or more particle images will be found in the search area. A solution to the presented problem is to reduce the tolerance width, which is a feature available in OpenPTV. Nevertheless, the reduction of these segments is not a warranty that all correspondences will be found. Let us look at Figure 2.7 again, if we reduce the search length in the epipolar line to half of the segment $\overline{XX_2}$ the algorithm can create two particles with different positions: X and X_2, but we will not be able to find correspondence for X_1, unless the distance is smaller than the segment $\overline{XX_1}$.

A better solution is to add another camera. By doing so, an extra epipolar

line segment can be defined. Each particle will be defined by the intersection of both epipolar lines in each image (H. Maas, Gruen, and Papantoniou 1993). We can conclude by this analysis that the 2 camera approach is not enough to visualize the bubble plume. We decided to use an array of four cameras to analyze the bubble plume. The results of this investigation are presented in Paper II

2.3 3D PTV setup for use with droplets

For the last part of this thesis, the setup was slightly modified to measure the droplets created after a breaking wave. The experiments were conducted in the wave tank of the Hydrodynamics Laboratory. The focus of the investigation is the production of droplets from different types of breaking waves. The main idea is to locate the area where the droplets are produced and adapt the camera array to fit the area. To do this, it is necessary to consider the camera and lenses specifications, the expected range of droplet size and the total area of analysis. A detail description on how to achieve this will be done below. As mentioned before, the selected software to analyze the data was OpenPTV.

The used cameras were AOS PROMON U1000 Mono cameras with an image size of 1080×1920 pixels. With an approximated range of droplets diameters from 0.1 mm to 10 mm, we have three orders of magnitude to consider in the image resolution. If we approximate that we want 0.3mm to be equivalent to 2 pixels, the diameter range can extend up to 70 pixels, which would be equivalent to 10.5 mm. The camera lenses had 50 mm focal distance. To obtain the desired pixel to millimeter scaling, the necessary distance between the focal plane (the center of the tank) and the cameras is approximately 1.72 m. To create the 3D field of view, there is a calibration procedure that should be accomplished. This

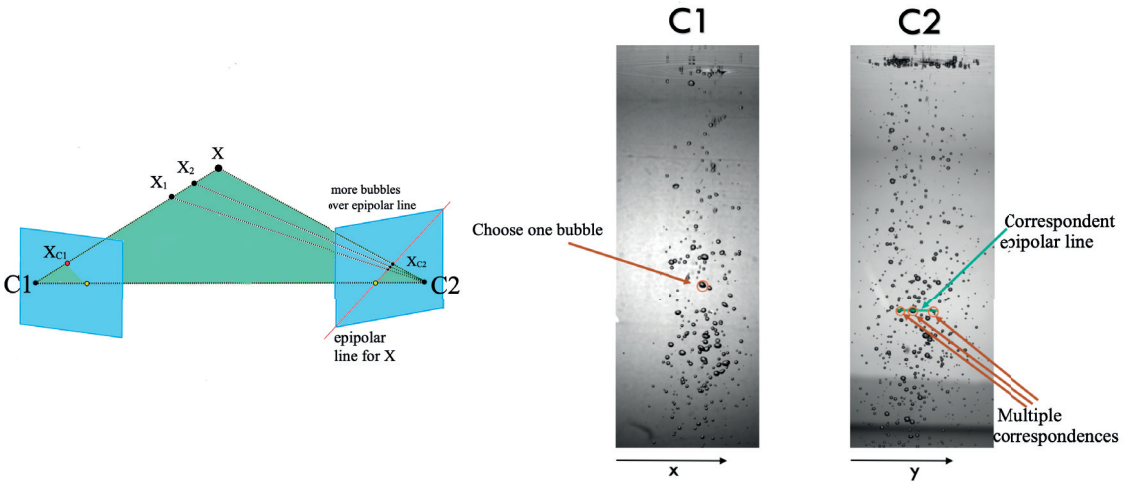

Figure 2.7: When analyzing bubbles, an array with only 2 cameras gives more than one correspondence because of the length of the epipolar segment.

calibration procedure requires the characteristics of the cameras, their positions and an approximation of the desired volume of investigation. Different types of calibration can be made in OpenPTV. In this study, calibration by multiple planes was made. The details of the procedure will be explained next.

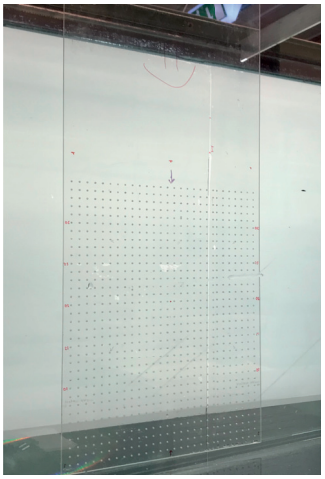

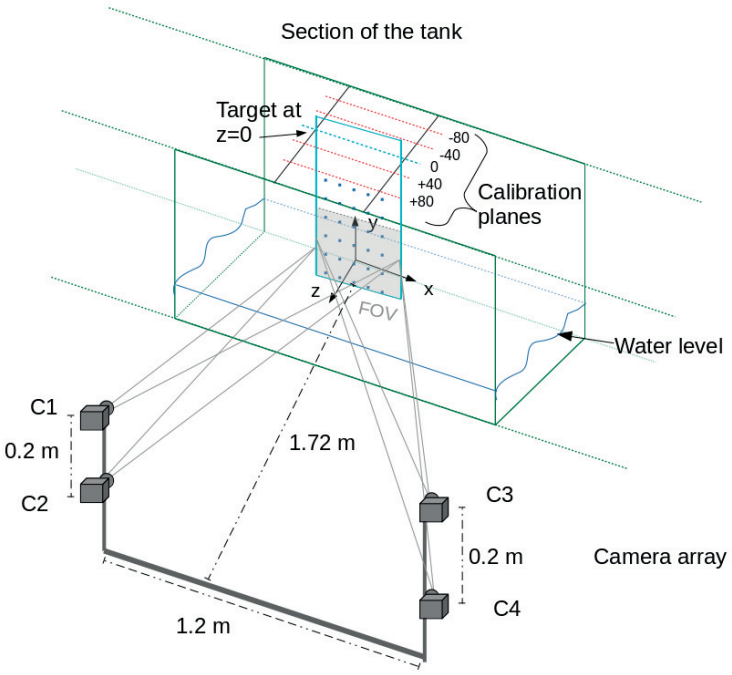

Figure 2.8: On the left, a picture of the calibration target. On the right, schematics of the target and cameras positions to create the calibration by multiple planes.

The multiple plane calibration consist on using a flat calibration target in several depth planes which will define the volume of analysis. The calibration target was an acrylic sheet of 3mm thickness with a mesh of 1mm holes, each hole was 10mm separated from its neighbors (fig. 2.8). The volume of analysis was defined by a Cartesian frame of reference (x, y, z) where the x direction moves along the tank, the y direction is the vertical direction and the z direction moves towards the cameras, perpendicular to the tank. The plane $z = 0$ was defined as the center of the tank and the origin $(0, 0, 0)$ was defined as the middle of the calibration target. Once the coordinate system was defined, the calibration target helped to define the cameras positions. The cameras should be all looking at the same volume from different angles. Because of the diffused light technique, the cameras could only be positioned at one side of the tank. The camera array is presented in Figure 2.8 and the positions of the cameras with reference to the origin of the system are shown in Table 2.1

The use of OpenPTV software will be necessary for the next steps. For more detailed instructions on the installation and use of the software, see the software page (OpenPTV et al. 2012). Below, a basic summary of the procedure to achieve the multiple plane calibration is described:

Camera	x[cm]	y[cm]	z[cm]
Camera 1 (C1)	−60	15.5	190
Camera 2 (C2)	−60	−10.5	190
Camera 3 (C3)	60	13.5	189
Camera 4 (C4)	60	−8.5	189

Table 2.1: Positions of the cameras in the camera array compared to the origin of the reference system.

1. Take images of the calibration target in the different planes. In this case, five planes were used corresponding to the planes: $z = -80,\ z = -40\ z = 0,\ z = 40, z = 80$ mm.

2. The images are an input to the calibration folder. The software requires that the data is separated in folders: one for the calibration objects, one for the parameters, one for the images of the moving particles and one for the results. The folders have to be created before using the program for the first time. It is important to have dummy parameter files already in the correspondent folders. For the multiple plane calibration we will also require several parameters folders, one for each calibration plane used.

3. Input the Cartesian position of the grid holes for each plane in a text file, for example: target_0.txt, target_m4.txt, target_p4.txt. The files should be organized in 4 columns with the number on the grid in the first column (numeration starts with 1, bottom to top, left to right), x location in the second column, y location in the third column, z location in the fourth column.

4. Use the files with the extension ".ori" to input the position of the cameras with respect to the origin and the approximated rotation angles with respect to the main axes x, y, z. In these files also the positions of the pinhole in respect to the image center in millimeters, the back-focal distance, and the position of the glass in respect to the origin are needed.

5. Choose 4 points in the target that are visible in each camera and collect their grid numbers(from the target_*nn*.txt files, *nn* refers to the chosen name) in a file called "man_ori.par" which should be in the parameters folders.

6. Follow the steps of the calibration as proposed by the tutorial. In our case, the most useful tutorial was the descriptions for the "Multi-Plane Calibration Procedure" presented in the *Tutorial written by Hristo Goumnerov*, available in the OpenPTV website OpenPTV et al. 2012. The main steps are:

    - Detect the grid points in each camera image

- Select the 4 points collected in the “man_ori.par" file
- Check the precision of the “.ori" files and modify them to accurately reproduce the grid
- Once the image grid is close to the estimated grid use the algorithm to refine the parameters and create the final version of the “.ori" files.
- Repeat for each plane
- Create the combined set of files that contains the information from all the planes

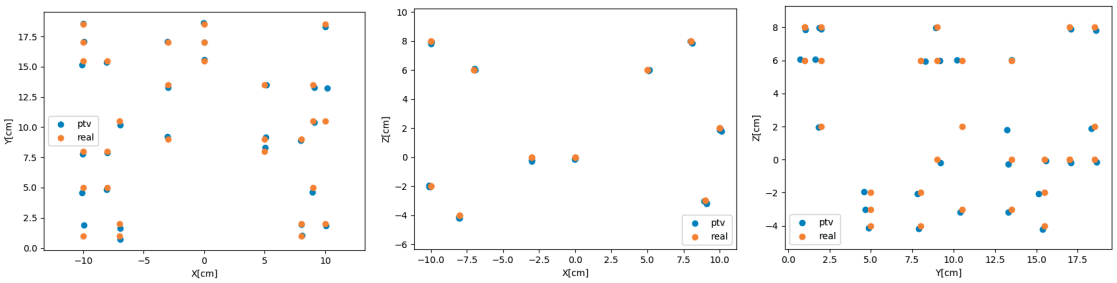

Figure 2.9: Results of using a particle array with known positions to compare with PTV results. The plots show the accuracy of the PTV in each projection plane. On blue dots the results from PTV are shown and in orange dots the real positions are shown.

Once the calibration was achieved, a small configuration can be used to confirm the precision of the calibration. In this study, a 3D grid of 30 particles with different sizes was created and used to test the precision of the calibration. The position of the particles in respect to the chosen origin is known. By using the OpenPTV software we obtained the positions as estimated by the algorithm and compared them with the known positions. The results are presented in Figures 2.9 and 2.10. These figures show that when the calibration is successful, the position of the particles can be tracked within an accuracy of 2 mm in all directions. If larger errors are found or the position do not correspond accurately in all cases, the most probable reason is an error during the calibration. The procedure should be revised and maybe even the cameras positions need to be improved.

An important contribution of the setup developed in this thesis, is the estimation of the sizes of the droplets. When conducting PTV measurements in general, the particle size is already known, or irrelevant. But in our study, it is one of the main unknown parameters that we want to extract from the data. The image processing done by the software saves information of the tracked particles and their pixel sizes for each camera and time step. Therefore it is possible to use this information to estimate the size of each particle and its evolution in time.

Because of the calibration process, it is possible to obtain an estimation of the pixel to world transform, including the size error depending on the particle

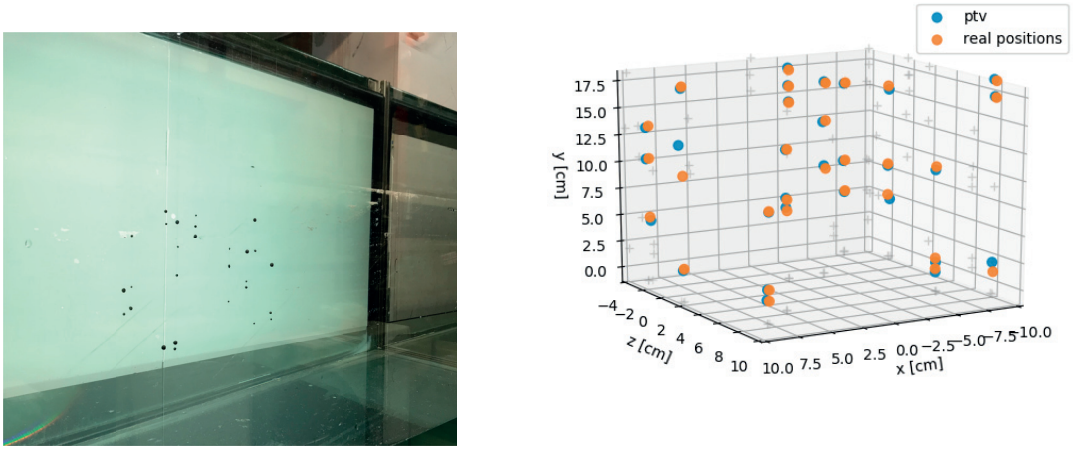

Figure 2.10: Results of using a particle array with known positions to compare with PTV results. On the left, a picture of the real particle array. To the right a 3D plot of the results is presented.

distance to the camera. In this thesis a simple approximation is made by calculating the pixel to millimeter scale S_i for each calibration plane i. Then, a second order fit is obtained according to the depth: $S(z) = c_2 z^2 + c_1 z + c$, where z is the z coordinate of the analyzed droplet. From the OpenPTV results, we can extract the pixel length in x and y of a droplet for each camera, called A_C and B_C respectively, where C stands for the camera: $C = 1, 2, 3, 4$. Then we obtain the average of these quantities and apply the defined transform: $\alpha_p = \overline{A_C} * S(z_p)$ and $\beta_p = \overline{B_C} * S(z_p)$, where z_p is the position of the droplet p in z and α_p and β_p are its calculated axes lengths. Finally using the definition of equivalent diameter: $D_e = \sqrt{(\alpha_p \beta_p)}$ we obtain the estimated diameter for the droplet p.

With the same configuration of 30 particles used to confirm the positions, a comparison of the real sizes of the particles can be made to those resulted from this calculation. The results are presented in Figure 2.11, where it is visible that the calculation can estimate the size of the particles within the constrains of the image resolution. In the figure, an error bar of 3 pixels, or 0.45 mm, is presented. In all cases, the size estimation lies within this error. It is interesting to notice that, in all cases, the calculation overestimates the size of the particle. This over estimation is reasonable from the image processing perspective, because blurry particles are perceived as bigger in an image.

With this proposed methodology, the tracking of droplets was performed. In this study, two different cases were analyzed. The first one was the study of the droplet production after a breaking wave, which is presented in Paper III. The second one is the study of droplet production by a solitary wave impacting in a flat vertical wall during different stages of breaking, which is presented in Paper IV.

Overall, a realistic estimation of positions and sizes can be performed by using this setup. There is also room for improvement. For example, more sophisticated

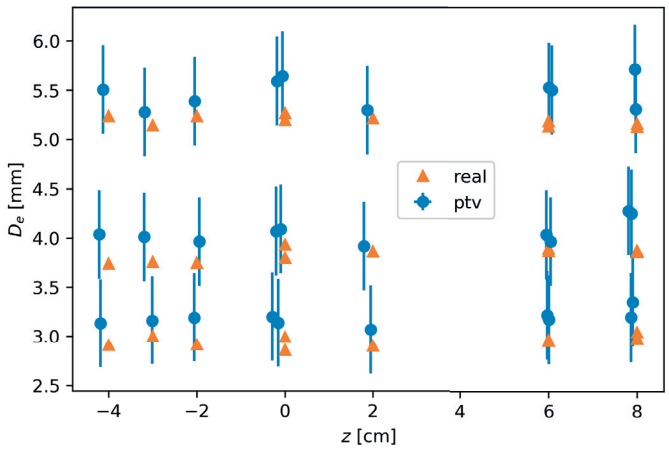

Figure 2.11: Results of the algorithm to determine particle size compared to the known sizes of the particle array. In blue circles, the estimated sizes with errorbars of 3-pixel length(= 0.45mm)are presented. In orange triangles, the measured equivalent diameters D_e are presented.

cameras and lenses could improve the image resolution, frame rate and shutter speed to obtain sharper images of the droplets. Especially in the size estimation, an interesting way to reduce the error could be to make a deeper study of the image-size relation using the camera and lens characteristics. In this way, an extra calibration procedure could be added to the software, when it is of interest to obtain particle sizes also.

Chapter 3

Objectives and findings in publications

Paper I The objective of this paper was to determine a relation between the naturally occurring disturbances on the jet surface and air entrainment. The usage of statistical analysis was the basic core of the found results. Our results show that both the bubble count and entrained air have a linear relation with the steepness of the jet disturbances. The developed imaging technique in this investigation gave the foundation for the next papers.

Paper II The second paper initiated an attempt to obtain three-dimensional results of the previous paper. Nonetheless, the complexity and abundance of the bubbles inside the plume made this work a technical paper on the design of the 3DPTV system for the bubble plume. The bubble kinematics were obtained and an analysis of the requirements to obtain reliable PTV measurements was made. Also, this investigation set the grounds for the experimental technique developed in the next papers.

Paper III A 3DPTV setup was achieved in order to measure droplet dynamics. The aim of this paper was to generate violent plunging breakers in the laboratory, quantify the produced droplets, obtaining their sizes and kinematics and to analyze the effect of the different wind speeds on the droplet production.

Paper IV A similar 3DPTV setup is used to analyze the droplet production from solitary waves impacting in a vertical wall. An extensive description of the experimental results is presented. The main contributions are the analysis of the wave breaking stage during the impact and the statistical analysis of size distributions, velocities and accelerations. This manuscript need to be further refined to be submitted into a peer reviewed journal.

Bibliography

Andreas, E. L. (2002). “A review of the sea spray generation function for the open ocean”. In: *Advances in Fluid Mechanics* vol. 33, pp. 1–46.

Andreas, E. L. et al. (1995). “The spray contribution to net evaporation from the sea: A review of recent progress”. In: *Boundary-Layer Meteorology* vol. 72, no. 1-2, pp. 3–52.

Biń, A. K. (1993). “Gas entrainment by plunging liquid jets”. In: *Chemical Engineering Science* vol. 48, no. 21, pp. 3585–3630.

Bodaghkhani, A. et al. (2016). “Understanding spray cloud formation by wave impact on marine objects”. In: *Cold Regions Science and Technology* vol. 129, pp. 114–136.

Bogaert, H. et al. (2010). “Sloshing and scaling: results from the Sloshel project”. In: *The Twentieth International Offshore and Polar Engineering Conference*. International Society of Offshore and Polar Engineers.

Borisenkov, Y. P. and Pchelko, I. (1975). *Indicators for forecasting ship icing*. Tech. rep.

Bredmose, H., Peregrine, D., and Bullock, G. (2009). “Violent breaking wave impacts. Part 2: modelling the effect of air”. In: *Journal of Fluid Mechanics* vol. 641, p. 389.

Bullock, G. et al. (2007). “Violent breaking wave impacts. Part 1: Results from large-scale regular wave tests on vertical and sloping walls”. In: *Coastal Engineering* vol. 54, no. 8, pp. 602–617.

Chanson, H., Aoki, S., and Hoque, A. (2006). “Bubble entrainment and dispersion in plunging jet flows: freshwater vs. seawater”. In: *Journal of Coastal Research*, pp. 664–677.

Chanson, H. (1996). *Air bubble entrainment in free-surface turbulent shear flows*. Elsevier.

Chanson, H., Aoki, S.-i., and Maruyama, M. (2002). “Unsteady air bubble entrainment and detrainment at a plunging breaker: dominant time scales and similarity of water level variations”. In: *Coastal Engineering* vol. 46, no. 2, pp. 139–157.

Cook, J. and Chatterton, M. N. (2008). “The Effects of Icing on Commercial Fishing Vessels”. In:

Deane, G. B. (1997). “Sound generation and air entrainment by breaking waves in the surf zone”. In: *The journal of the acoustical society of America* vol. 102, no. 5, pp. 2671–2689.

Deike, L., Melville, W. K., and Popinet, S. (2016). “Air entrainment and bubble statistics in breaking waves”. In:

Dias, F. and Ghidaglia, J.-M. (2018). “Slamming: Recent progress in the evaluation of impact pressures”. In: *Annual Review of Fluid Mechanics* vol. 50, pp. 243–273.

Dommermuth, D. G. et al. (2007). *An application of cartesian-grid and volume-of-fluid methods to numerical ship hydrodynamics*. Tech. rep. SCIENCE APPLICATIONS INTERNATIONAL CORP SAN DIEGO CA.

Fairall, C. et al. (2009). “Investigation of the physical scaling of sea spray spume droplet production”. In: *Journal of Geophysical Research: Oceans* vol. 114, no. C10.

Hattori, M., Arami, A., and Yui, T. (1994). “Wave impact pressure on vertical walls under breaking waves of various types”. In: *Coastal Engineering* vol. 22, no. 1-2, pp. 79–114.

Hull, P. and Müller, G. (2002). “An investigation of breaker heights, shapes and pressures”. In: *Ocean Engineering* vol. 29, no. 1, pp. 59–79.

Jensen, A. (2019). “Solitary wave impact on a vertical wall”. In: *European Journal of Mechanics-B/Fluids* vol. 73, pp. 69–74.

Kiger, K. T. and Duncan, J. H. (2012). “Air-entrainment mechanisms in plunging jets and breaking waves”. In: *Annual Review of Fluid Mechanics* vol. 44, pp. 563–596.

Kolaini, A. R. (1998). “Sound radiation by various types of laboratory breaking waves in fresh and salt water”. In: *The Journal of the Acoustical Society of America* vol. 103, no. 1, pp. 300–308.

Lafeber, W., Bogaert, H., Brosset, L., et al. (2012). “Elementary Loading Processes (ELP) involved in breaking wave impacts: findings from the Sloshel project”. In: *The Twenty-second International Offshore and Polar Engineering Conference*. International Society of Offshore and Polar Engineers.

Lamb, H. (1932). *Hydrodynamics*. The University Press.

Lenain, L. and Melville, W. K. (2017). “Evidence of sea-state dependence of aerosol concentration in the marine atmospheric boundary layer”. In: *Journal of Physical Oceanography* vol. 47, no. 1, pp. 69–84.

Lozano, A., Garcıa-Olivares, A., and Dopazo, C. (1998). “The instability growth leading to a liquid sheet breakup”. In: *Physics of fluids* vol. 10, no. 9, pp. 2188–2197.

Lozowski, E. P., Szilder, K., and Makkonen, L. (2000). “Computer simulation of marine ice accretion”. In: *Philosophical Transactions of the Royal Society of London. Series A: Mathematical, Physical and Engineering Sciences* vol. 358, no. 1776, pp. 2811–2845.

McKeogh, E. and Ervine, D. (1981). “Air entrainment rate and diffusion pattern of plunging liquid jets”. In: *Chemical Engineering Science* vol. 36, no. 7, pp. 1161–1172.

Meerkerk, M. van et al. (2020). “Experimental investigation of wave tip variability of impacting waves”. In: *Physics of Fluids* vol. 32, no. 8, p. 082110.

Maas, H.-G. (1991a). “Automated photogrammetric surface reconstruction with structured light”. In: *Industrial Vision Metrology*. Vol. 1526. International Society for Optics and Photonics, pp. 70–77.

— (1991b). “Digital photogrammetry for determination of tracer particle coordinates in turbulent flow research”. In: *Photogrammetric Engineering & Remote Sensing* vol. 57, no. 12, pp. 1593–1597.

Maas, H., Gruen, A., and Papantoniou, D. (1993). “Particle tracking velocimetry in three-dimensional flows”. In: *Experiments in fluids* vol. 15, no. 2, pp. 133–146.

O’Dowd, C. D. et al. (2008). “A combined organic-inorganic sea-spray source function”. In: *Geophysical Research Letters* vol. 35, no. 1.

OpenPTV, C. et al. (2012). *OpenPTV: Open source particle tracking velocimetry*. https://www.openptv.net. [Online; accessed 20-December-2020].

Oumeraci, H. et al. (2001). *Probabilistic design tools for vertical breakwaters*. CRC Press.

Rashid, T., Khawaja, H. A., and Edvardsen, K. (2016). “Review of marine icing and anti-/de-icing systems”. In: *Journal of Marine Engineering & Technology* vol. 15, no. 2, pp. 79–87. eprint: https://doi.org/10.1080/20464177.2016.1216734.

Roisman, I. V., Horvat, K., and Tropea, C. (2006). “Spray impact: rim transverse instability initiating fingering and splash, and description of a secondary spray”. In: *Physics of Fluids* vol. 18, no. 10, p. 102104.

Ryerson, C. C. (1990). “Atmospheric icing rates with elevation on northern New England mountains, USA”. In: *Arctic and Alpine Research* vol. 22, no. 1, pp. 90–97.

Sarchami, A., Ashgriz, N., and Tran, H. (2010). “An atomization model for splash plate nozzles”. In: *AIChE journal* vol. 56, no. 4, pp. 849–857.

Veron, F. (2015). “Ocean spray”. In: *Annual Review of Fluid Mechanics* vol. 47, pp. 507–538.

Villermaux, E., Marmottant, P., and Duplat, J. (2004). “Ligament-mediated spray formation”. In: *Physical review letters* vol. 92, no. 7, p. 074501.

Wang, H., Bertola, N., and Chanson, H. (2016). “Bubble entrainment in vertical plunging jets”. In: *Australasian Fluid Mechanics Conference*. Australasian Fluid Mechanics Society, pp. 459–1.

Watanabe, Y. and Ingram, D. (2015). “Transverse instabilities of ascending planar jets formed by wave impacts on vertical walls”. In: *Proceedings of the Royal Society A: Mathematical, Physical and Engineering Sciences* vol. 471, no. 2182, p. 20150397.

— (2016). “Size distributions of sprays produced by violent wave impacts on vertical sea walls”. In: *Proceedings of the Royal Society A: Mathematical, Physical and Engineering Sciences* vol. 472, no. 2194, p. 20160423.

Wemmenhove, R. et al. (2015). “Numerical simulation of hydrodynamic wave loading by a compressible two-phase flow method”. In: *Computers & Fluids* vol. 114, pp. 218–231.

Wienke, J. and Oumeraci, H. (2005). “Breaking wave impact force on a vertical and inclined slender pile—theoretical and large-scale model investigations”. In: *Coastal engineering* vol. 52, no. 5, pp. 435–462.

Yuen, M.-C. (1968). “Non-linear capillary instability of a liquid jet”. In: *Journal of Fluid Mechanics* vol. 33, no. 1, pp. 151–163.

Zhu, Y., OĞUZ, H. N., and Prosperetti, A. (2000). “On the mechanism of air entrainment by liquid jets at a free surface”. In: *Journal of Fluid Mechanics* vol. 404, pp. 151–177.

Papers

Paper I

Experiments on air entrainment produced by a circular free falling jet

Reyna Guadalupe Ramírez de la Torre, Miroslav Kuchta, Atle Jensen

Published in *International Journal of Multiphase Flow*, August 2020, volume 132, 103424, ISSN 0301-9322, DOI: 10.1016/j.ijmultiphaseflow.2020.103424.

International Journal of Multiphase Flow 132 (2020) 103424

Contents lists available at ScienceDirect

International Journal of Multiphase Flow

journal homepage: www.elsevier.com/locate/ijmulflow

Experiments on air entrainment produced by a circular free falling jet

R.G. Ramirez de la Torre[a,*], Miroslav Kuchta[b], Atle Jensen[a]

[a] Department of Mathematics, University of Oslo, Norway
[b] Simula Research Laboratory, Fornebu, Norway

ARTICLE INFO

Article history:
Received 18 November 2019
Revised 1 July 2020
Accepted 9 July 2020
Available online 1 August 2020

Keywords:
Air entrainment
Wave steepness

ABSTRACT

The process of a circular free falling jet entering an idle pool was studied with the objective of determining a relation between the naturally occurring disturbances on the jet surface and air entrainment. To this end the instabilities of the free falling jet were characterized and compared with the bubble count distribution and an estimated amount of entrained air in the plume. Different jet lengths were considered. The aeration process was captured through image sequences. Individual analysis of each disturbance in the jet surface was made. Our results show that both the bubble count and entrained air have a linear relation with the steepness of the jet disturbances. Moreover, the wave-jet ratio is introduced, which defines an entrainment condition for all the studied cases.

1. Introduction

A large range of environmental processes entails complex two phase flow interactions. Most interactions in the atmosphere and marine surface occur between air and water. In the marine surface, these type of phenomena generate the aeration of the ocean by entrainment of bubbles underwater and the air-sea interactions by the creation of aerosol over the surface. A relatively simpler model of the interaction is the impingement of a jet in a pool. In the present study we are interested in wave breaking and marine icing processes. Here the size distributions of droplets and bubbles are important because the different sizes get transported differently in the marine boundary layer. In the case of droplets, small droplets can be transported over long distances and remain in the atmosphere for several days, while large droplets remain close to the ocean surface and return to the ocean in shorter times but still affect the air-sea fluxes of momentum and enthalpy (Veron, 2015). In the case of bubbles, the small bubbles reach larger depths and remain submerged for longer times thus contributing to the aeration of the ocean. On the other hand, the large bubbles penetrate only up to a certain depth. Therefore they contribute to the mixing of the top layer and generation of small aerosol when bursting on the surface (Chanson et al., 2006).

Mechanisms of a jet penetrating into a pool are relevant for understanding several of the phenomena mentioned above. Experimental and theoretical studies have therefore been made to address the system. Due to different objectives of the studies different (experimental) approaches have been used and different parameter ranges have been explored. We review some of the works in the following. Descriptions of the entrainment process have been made by Kiger and Duncan (2012), Zhu et al. (2000), McKeogh and Ervine (1981). It is generally acknowledged that the air entrainment process is controlled by several parameters. For the circular jet, the geometry of the nozzle will determine the behavior of the liquid flow. The flow instabilities are one of the primary producers of the disturbances. In several experimental studies, once a nozzle geometry is defined, the most commonly used parameter to address the entrainment threshold is the velocity of the jet (Chanson et al., 2006; Wang et al., 2016). Kiger and Duncan (2012) made a thorough compilation of previous results and described the process before and after the entrainment threshold. The critical condition for air entrainment can occur in different ways. In one case, there are no disturbances on the jet surface; only a meniscus is present which breaks when the steady-state is no longer possible. In the other case, the interface is destabilized by the disturbances within the impinging jet and/or receiving pool causing the meniscus to break. The last case can be further divided into case (i) with small disturbances such that the jet appears smooth and laminar, and case (ii) with disturbances such that the jet appears visibly rough. The type of air entrainment that was observed in the present work was of class (ii). Based on the observations and previous results, water and air systems are always within the low-viscosity regime with critical air entrainment conditions for $Re \sim 2000$. Other criterion to classify the entrainment conditions was to consider when the jet separated into droplets before entering the surface. Biń (1993) summarized the data available for

* Corresponding author.

https://doi.org/10.1016/j.ijmultiphaseflow.2020.103424

both cases. The main conclusion was that the droplet regime was well correlated to a Weber number power law but there was no strong or reliable correlation for the continuous jet regime.

The experiments in this study concentrated on low-viscosity, continuous jet regime where the air entrainment is caused by disturbances on the jet surface. The same entrainment regimes have been considered in several works. Davoust et al. (2002) and El Hammoumi et al. (2002) analyzed a circular falling jet in a similar regime to the experiments developed in this study. They use the dynamic jet roughness at the nozzle exit as a measure of the upstream hydrodynamic perturbations and a non-dimensional analysis that correlates the entrainment Weber number with the entrained air flow. In particular, the ratio of the nozzle diameter to its length, $L_c = L_{nozzle}/D_{\text{out}}$, is used to estimate the nature of the flow when exiting the nozzle (Kusabiraki et al., 1992). Davoust et al. (2002) also remarks that the stability theories developed until now do not succeed in describing air entrainment during the transition since the jet is highly sensitive to all external disturbances experienced by the liquid flow.

Arguably, the most similar experiment found in the literature is Oguz (1998). Therein the authors developed experiments of a jet with controlled water and air inflow. The imaging of the jet surface is used to quantify the surface roughness. In the study, authors used three different nozzle types, but made most of their analysis with a conical nozzle, which according to the authors provides a suitable option for the study. Their nozzle and jet dimensions gave Froude numbers one order of magnitude larger than presented here. The authors controlled both the air and water flow and the length of the jet was determined by these inflows, ranging from an intermittent jet with big pockets of air, to a stable jet with entrainment of small bubbles. As the main result of the study, the relevance of the shape of the surface disturbances in the process of air entrainment is shown by obtaining a relation of the wavelength of the disturbances with the maximum bubble radius encountered.

Eggers and Villermaux (2008) have made a thorough review of the physics of the jet. The majority of the work was concerned with the break up length and the breakup time for different flow regimes. In contrast, there has been little discussion about how the initial conditions affect the solutions of the proposed equations. However, (Wang et al., 2016; Lin and Reitz, 1998) note on high sensitivity of the solutions to the initial conditions. In experimental works (Davoust et al., 2002; El Hammoumi et al., 2002; Lin and Reitz, 1998; Oguz, 1998) it is found that the initial conditions for the jet, such as the nozzle exit geometry and the velocity profiles at the exit nozzle, have also high impact on the development of the disturbances on the jet surface.

This study presents a set of experiments that analyze a regime that, to the best of the authors knowledge, has not been thoroughly studied previously. With a very simple set-up we studied a fully turbulent jet in a considerably long pipe, which is only a single diameter plastic tube *without* a nozzle ($L_c = 66.67$) and different jet lengths (l) are considered. Furthermore, by controlling only the water flow we expect to show that the development of the disturbances is mainly due to flow instabilities, despite the complexity and randomness of the process. Therefore, the surface ripples are monitored until the moment the jet impacts the free surface. The individual amplitudes and wavelengths are measured to obtain a steepness distribution of the disturbances. This distribution and the significant wave height are used to characterize their development. Finally, the steepness is related to the entrainment and aeration.

2. Experimental methods

The experiments were conducted in a small tank with dimensions 1.50 m × 0.40 m × 0.40 m, as shown in Fig. 1. The water was

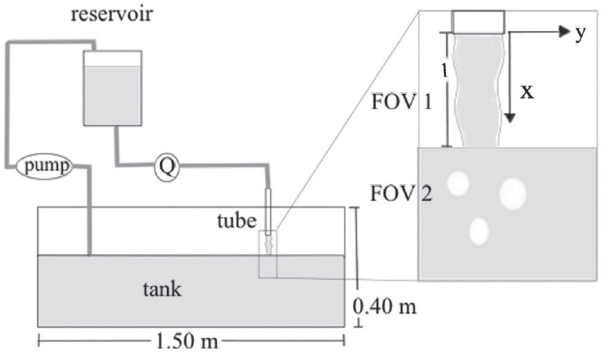

Fig. 1. Schematic experimental setup. The distance of interest l is measured from the outlet of the tube to the surface of the water.

stored in a movable reservoir and the flow rate of the water was changed by adjusting the height of the reservoir. The water drained freely through a flexible 0.6 cm plastic hose. To measure the flow, a IFM SM4000 flowmeter was used with a measuring range from 0 to 3 liters per minute and an accuracy of 2%. Downstream of the flowmeter, the water continued to travel through the hose until it reached the plastic tube of 40 cm in length and 0.6 cm in diameter, placed perpendicular to the water surface in the tank. The hose contained two smooth bends separated by a horizontal section where the flow meter was installed (cf. Q location in Fig. 1). The transition between the hose and the tube was smooth in shape as both parts had the same diameter but there was a change in the materials which implies a different behaviour near the walls. Three different distances between the outlet of the tube and the water surface were tested: $l = 2$ cm, 4 cm and 6 cm. Further, flow rates (Q) between 1.35 and 2.33 liters per minute were used. In the tank, the water level was kept constant using a pump to take the water back into the reservoir. The pump was off during the measurements to avoid undesired effects such as external currents or vibrations in the surface.

Images were used to capture the falling jet and the air entrainment underwater. The images of the jet were obtained with a Photron FASTCAM SA5 camera. The frame rate was 500 FPS with 1/2000 ms of shutter speed. Here the image resolution was 640 × 1024 pixels. The Field of View (FOV1) was approximately 2 cm × 1.25 cm. The recordings were 20 seconds long with a total of 10,000 generated images. Another set up of cameras was used to simultaneously capture images of the jet and the entrainment underwater. Two AOS Promon U1000Mono cameras were used. These cameras were synchronized at 500 FPS, with 1/500 ms shutter and with resolution 608 × 800 pixels. The Field of View was 3 cm × 2.28 cm. The FOV1 was centered at the jet falling while FOV2 was centered in the confluence area under the pool surface. All the cameras were synchronized to start recording with the flowmeter. Finally, the illumination was provided by LED lamps and the light was diffused with white plastic sheets and diffuser sheets.

For the present study, the disturbances on the jet surface and the air entrained under the surface were analyzed separately. As the disturbances present in the surface were uncontrolled, it is expected for them to have random behaviour. Therefore, careful record of the amplitude a, wavelength λ, and frequency f of the disturbances was made. The edges of the jet were extracted from the images by means of Sobel filtering and collected in a spatiotemporal array $y(x, t)$ encoding edge distance y at streamwise coordinate x and time t, cf. Fig. 2. The mean surface level was defined by averaging the data set in time: $\xi(x) = \overline{y(x,t)}$. Then, the wave height was obtained by subtracting the mean surface level: $\eta(x,t) = y(x,t) - \xi(x)$. A wavelength ($\lambda$) in η was defined as the

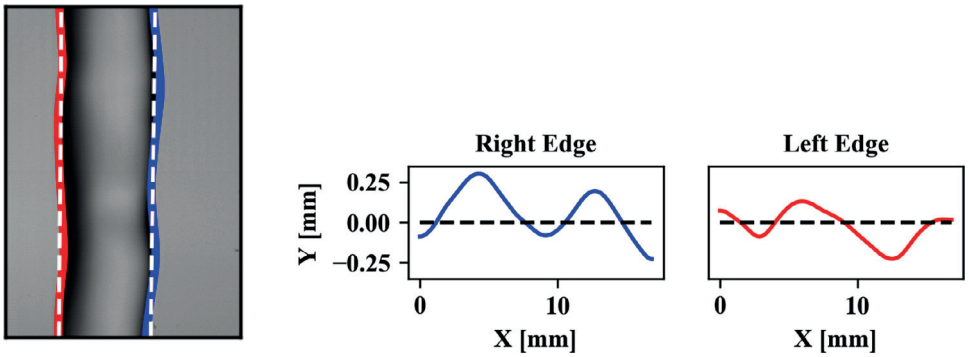

Fig. 2. Edge extraction process.

length from trough to trough and the amplitude (a) of the wave was defined as the height of the crest between the troughs.

To characterize the disturbances we used the wave steepness, ak, where $k = 2\pi/\lambda$ is the wave number. The wave steepness was obtained individually for every complete wavelength in the series, i.e. for every 2 consecutive troughs in a time step, a and λ are measured and an individual ak is calculated. The main objective was to obtain a relation between the disturbances in the jet and the quantity of air entrained.

From the subsurface point of view, a method to estimate the quantity of air entrained was needed. The most commonly used technique appears to be the use of intrusive probes to estimate the size and the number of bubbles in the generated plume (Chanson et al., 2006; Wang et al., 2016; Deane, 1997). One important advantage of the probes is the good estimation of the size distribution. Some of the disadvantages are then that the intrusive instrument can affect the development of the phenomenon and that the size of the probe determines a threshold in the possible measured sizes. Here, we have therefore opted for the use of high speed imaging. This technique is non intrusive and with the adequate instrumentation can have a higher size resolution. When the plume density is scarce, i.e. there are very few overlapping bubbles, the videos provide high accuracy data. On the other hand, in a dense plume the overlap of the bubbles limits the number of visible bubbles. To solve this problem it is possible to use more than one camera at different angles of the plume. However, in this set of experiments one camera is used due to the low number of bubbles generated in the pool. We remark that for the case with larger Reynolds number and jet length ($l = 6$ cm), the bubble count can be affected by these effects.

Using the images, an estimate of the entrained air and the number of bubbles were obtained as follows. The bubbles were identified with a threshold and using a routine to find enclosed areas, known as contours. Then their shape was approximated by an elliptic contour from which the area was determined. The entrained air will be estimated only by the visible area occupied by air in the image. The area is computed as πab with a the major axis and b the minor axis of the ellipse obtained. In this way, statistics of the entrained air area and bubble counts were made for each of the analyzed cases. To obtain a non-dimensional value of the entrained air we use the area fraction

$$\alpha = \frac{A_{\text{bubbles}}}{A_{\text{water}}},$$

where the area of bubbles is the sum of all the bubble areas found and the water area is the total area in the image FOV.

3. Dimensional analysis and description of the process

For each falling distance l we have a range of flow rates Q. For each Q, we can obtain an outlet velocity (V_{out}) and estimate a falling velocity at the confluence point (V_{jet}) with the equations

$$V_{\text{out}} = \frac{Q}{A}, \quad V_{\text{jet}} = \sqrt{V_{out}^2 + 2gl}, \tag{1}$$

where A is the cross section area of the tube and g is gravity acceleration.

For this work the relevant dimensionless parameters are the Reynolds, Froude and Weber numbers, which respectively describe the relative importance of inertial forces and viscous forces in the jet, the inertial forces and gravitational forces on the surface of the jet and inertial forces and surface tension. From the calculated velocities we can obtain Reynolds numbers for the outlet flux (Re_{out}) and estimate a Reynolds number for the falling jet (Re_{jet}). These Reynolds numbers are defined according to

$$Re_i = \frac{V_i D_i}{\nu}, \tag{2}$$

where ν is the dynamic viscosity of water, D_{out} is the diameter of the tube and D_{jet} is the diameter of jet at the confluence point. For the falling jet we define the Froude number

$$Fr = \frac{V_{\text{jet}}^2}{gD_{\text{jet}}}. \tag{3}$$

Weber numbers can be obtained for the amplitude of the disturbances and for the bubble size distribution

$$We_i = \frac{\rho V_{\text{jet}}^2 \epsilon_i}{\sigma}, \tag{4}$$

where ρ is water density, σ is the surface tension for air and water interface and ϵ_i is the adequate length scale. For the jet Weber (We_{jet}), it is the amplitude of the disturbances, while for the bubble Weber (We_{bub}) the individual bubble diameter is used. The range of bubble Weber numbers obtained here is based on considering the smallest and the largest bubbles found during the analysis. These parameters can be found in Table 1.

Table 1
Relevant non-dimensional parameters for each falling distance l.

l (cm)	Re_{out}	Re_{jet}	Fr	We_{jet}	We_{bub}
2	4800-8200	5000–7600	21–46	4.6–10	11-137
4	4900-8200	5500–8000	29–54	8.7–16	9-155
6	4900-8200	5800–8500	37–62	16.6–24.4	57-158

There are 2 parameters that are important in the generation of the disturbances from the exit: Re_{out} and L_c both define the flow regime in the tube and its stability. Based on the Reynolds number the flows are fully turbulent. Furthermore, the ratio L_c points to a fully developed flow. In addition we consider a relation of the two parameters which shows the possibility that the boundary layer inside the tube is unstable, generating the disturbances on the jet

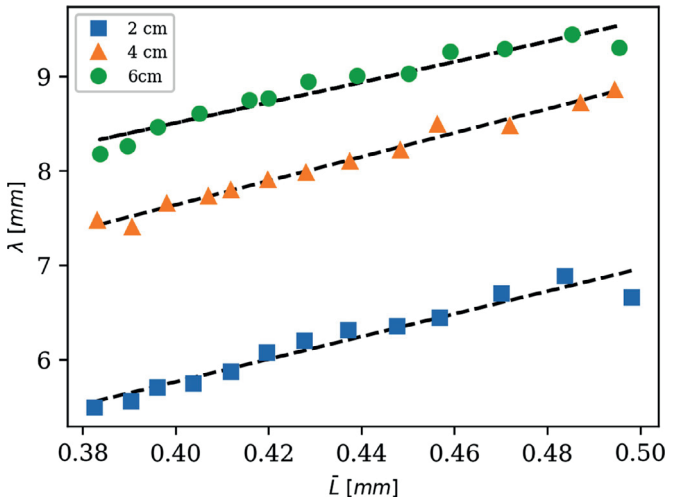

Fig. 3. Theoretical boundary layer thickness against the wavelength of the disturbances. Dashed lines represent the equations $\lambda = C\delta_1$. Here, values of C varies between (6.28, 7.38) while in Oguz (1998) C =15.7, 17.5 are reported.

surface

$$\frac{L_c}{Re_{\text{out}}} = \frac{L_{\text{tube}}\nu}{V_{\text{out}}D_{\text{out}}^2} = \frac{\bar{L}^2}{D_{\text{out}}^2}, \tag{5}$$

where $\bar{L} = (\nu\bar{x}/V)^{1/2}$ is the boundary layer thickness (Reed et al., 1996). This ratio defines the size of the boundary layer compared to the diameter of the tube, which indicates that the boundary layer is completely developed if

$$\sqrt{\frac{L_c}{Re_{\text{out}}}} > 0.5.$$

In our case the ratio goes from 0.083 to 0.063, which means the boundary layer occupies between 12–17% of the flow width and it would thus be reasonable to assume the boundary layer instability is responsible for the creation of the disturbances at the surface. As proposed by Dai et al. (1997) and confirmed by Oguz (1998) we can relate the momentum thickness to the wavelength of the disturbances and use the Blasius boundary layer stability analysis to obtain the lowest unstable wavelength at the onset using:

$$\lambda = C\delta_1, \quad \delta_1 = 1.72\bar{L} \tag{6}$$

where δ_1 is the displacement thickness. As shown in Fig. 3 the relation is fulfilled in all the presented cases in this work, but the value of C is different compared to those presented in the literature (Oguz, 1998). This difference can be due to nozzle geometry or different values for L_c, Re_{out}, compared to the mentioned studies. Different materials will also change the wettability. This is elaborated in Appendix A, where results are shown for additional measurements using a glass pipe in the setup.

During the free fall of the jet, the forces that can be relevant on the surface deformation are gravity, surface tension, viscous stresses and pressure. First we can recall the results on Table 1 where, from the range of Froude numbers, it is obvious that gravity will not play an important role in the development of the disturbances. Furthermore, since Reynolds number is high for all cases, inertia is more relevant than viscous stresses. To estimate the importance of the external pressure compared to the surface tension we look at the Weber numbers of the jet, which show that the inertia of the waves is strong enough to deform the surface and increase their amplitude. Finally, comparing these two parameters with each other, we obtain a capillary number

$$Ca = \frac{We_{jet}}{Re_{\text{jet}}} = \frac{\mu V_{\text{jet}}}{\sigma}, \tag{7}$$

that is, a measure of the capillary force against the viscous stress. From the values in Table 1, we calculate the largest capillary number to be $Ca = 0.005$, we can immediately see that surface tension will be dominant. Therefore, the most relevant forces will be surface tension and inertial stresses given by the pressure balance at the interface. The surface tension is enough for the jet not to break into smaller bulks of water, but the internal pressure is enough to allow growth of the waves at the surface of the jet.

As for the entrainment, the obtained Weber number shows that the disturbances are capable of creating an over-pressure upon the free surface. In this way the free surface is also deformed and allows the creation of the air cavity which will grow downwards due to the velocity of the jet. However, according to Bin (1988) and Biń (1993), there is no successful theoretical approach for predicting the critical entrainment velocity for a vertical plunging jet. For that reason, experimental measurements have been used with reasonable confidence to define a threshold. In Cummings and Chanson (1999), Chanson et al. (2006), Wang et al. (2016), the onset velocity for air entrainment was defined as the velocity where one to five bubbles are entrapped during a certain period depending on the geometry of the problem (order of minutes). This definition has been considered for plunging jets, which means that the jet starts with its goal velocity and hits the surface of the pool before merging and generating aeration. The experiments developed for this study do not consider jets that plunge on the surface. Instead, the jet hits the surface during the non entrainment regime and the jet velocity is augmented gradually until the final value. For this reason, a new onset definition was required which took into account the jet-pool interaction. More details on the procedure and the definition of the threshold will be given in the Results section.

4. Results and discussion

The phenomena described in the present work is similar to studies in Kiger and Duncan (2012), Zhu et al. (2000), McKeogh and Ervine (1981). In particular, the most suitable regime would be the one addressed as transition to turbulent jet Oguz (1998). Nonetheless, the present study shows experiments both with and without entrainment. All of the jets considered herein had disturbances at the surface, but only a group of them created air entrainment. In Fig. 4, one of the typical entrainment situations is presented. When a disturbance is steep enough, it creates an air pocket that is pulled down with the velocity of the jet and the subsequent disturbances help to close the air cavity behind. There is a similarity between this image sequence and the sketches presented in Oguz (1998). It is also a confirmation that the front of the wave is responsible for the entrainment as suggested by Zhu et al. (2000) and Ohl et al. (2000).

The growth of the waves is visualized in Fig. 5 a, where the significant wave height H_s, as defined in wave theory (4 times the standard deviation of the time average signal in each point), has been plotted for the length of the jet in the last two centimeters of all the cases with a similar Re_{out}. It is visible that the longer the fall, the more developed the disturbances are. This figure shows statistically that there is an amplitude increase in the disturbances while falling down the jet and that the increase is independent of the radial position, i.e. similar results are obtained for the left and the right edge. Although, when looking at the data instantaneously, evidence of superposition of frequencies is visible, such as local minima or maxima traveling along the fall length which supports the hypothesis that the presented disturbances are random.

While the images revealed that the falling jet was not axisymmetric, Fig. 5 shows that both edges exhibit similar statistical behaviour. Fig. 5 a shows comparable amplitude increment with the jet length. Further, in Fig. 5 b the same conclusion can be drawn for the steepness. In addition, it can be interpreted from Fig. 5 b

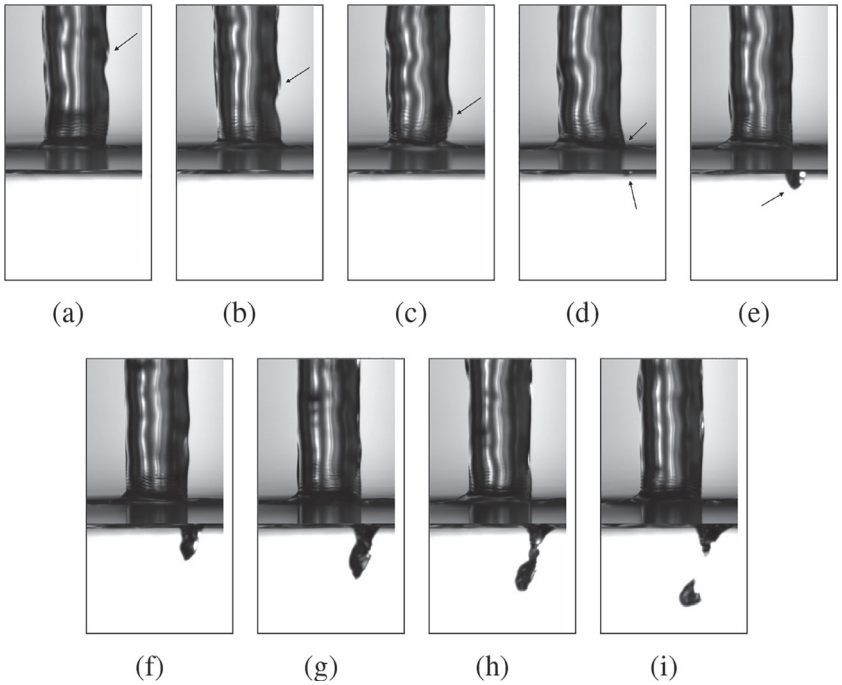

Fig. 4. Sequence of images showing a steep wave (indicated by arrow) on the jet surface generating a bubble while crossing the free surface.

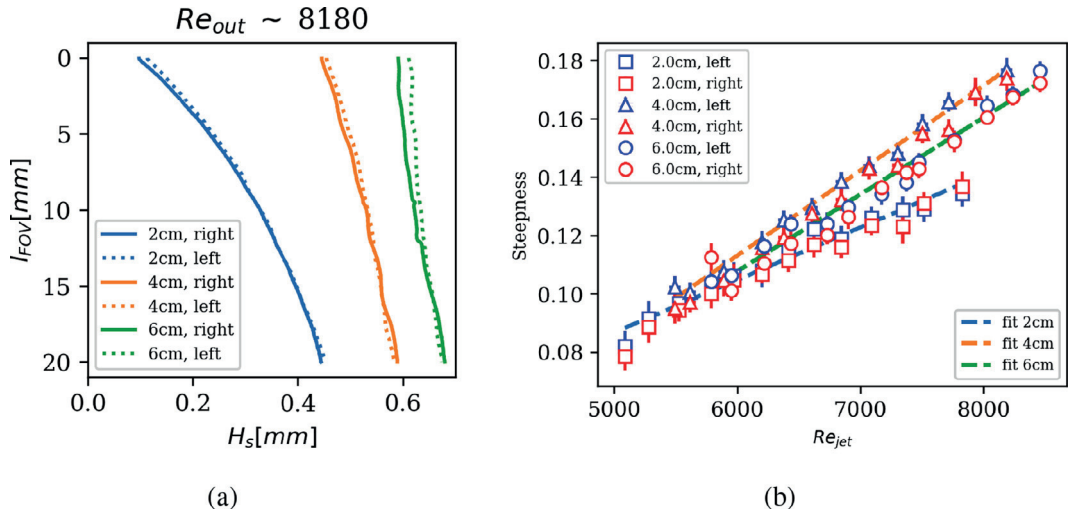

Fig. 5. (a) Significant wave height (H_s) against falling distance. Only the 2 cm closest to the free surface are analyzed. The different line styles differentiate between right and left edge. (b) Mean steepness for the different cases and both edges of the jet. The blue color represents the left edge and the red color represents the right edge. Linear fits are represented with dashed lines. It is visible that the mean steepness increases with the Reynolds number of the falling jet. (For interpretation of the references to color in this figure legend, the reader is referred to the web version of this article.)

that the last case with $l = 6$ cm presents a change in the waves characteristics; a decrease of the steepness for higher Reynolds number is noticeable compared to $l = 4$ cm. This figure shows that for large l, the amplitude increases. It is further possible to conclude that there is a decrease in k and therefore an increase in λ for the case of $l = 6$ cm. This result could be an indication that the characteristics of the waves depend on the length of the jet. In other words, having a bounded domain can affect the expected λ spectra compared with the theory (Lamb, 1993, art. 273), which consider the case of an infinite jet length. In contrast, by following a crest through its path, we find evidence that the disturbances travel along the jet at the same speed as the falling jet as this theory indicates.

In Figs. 6 and 7 the steepness distributions are shown for different Reynolds numbers. In all cases, the steepness distribution was a skewed distribution, which means that the steepness is not Gaussian distributed. The skewness is a measure of the asymmetry of the distribution, being 0 for the case of a Gaussian distribution. In all the cases, the skewness was close to 1. Another statistical parameter used to identify the distributions is the kurtosis, which is a measurement of the quantity of extreme events present. For a Gaussian distribution, the kurtosis is 3, for all the cases presented here, the kurtosis was close to 5. We note that the shape of these distributions is similar to the distributions reported in Jiang et al. (2008) and Tayfun (2006) which concern free surface waves in the ocean.

In Fig. 6 the distribution of the steepness can be compared with the distance the jet has fallen. If the total falling distance is divided in two equal parts, the analysis can be done in each half separately. It is observed that the waves in the first half, closer to the

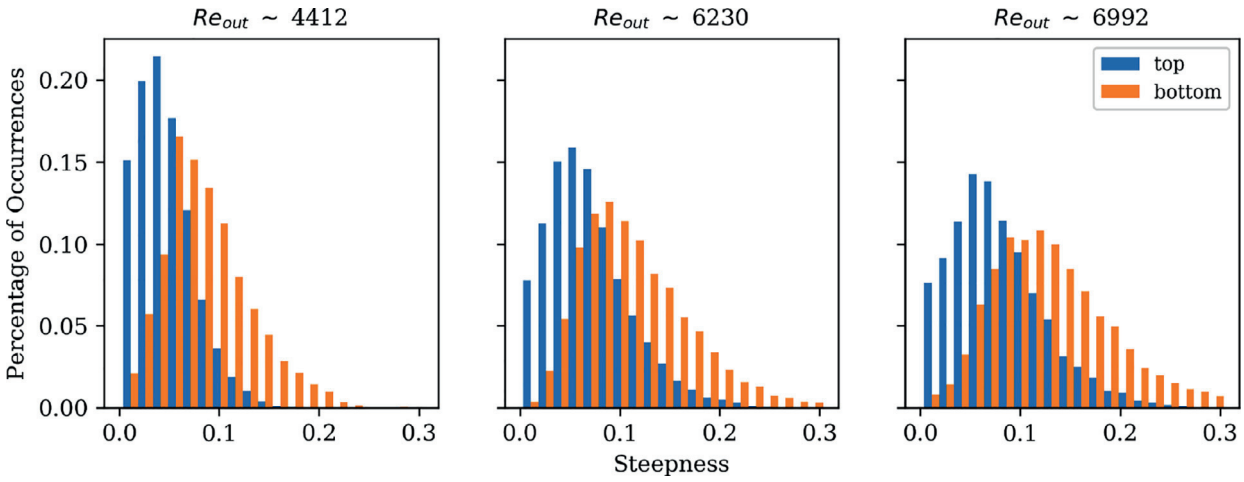

Fig. 6. Distribution of the steepness of the waves during the free fall. Results for $l = 4$ cm are shown. The label top refers to the top 2 cm, i.e. closest to the outlet. The label bottom refers to the bottom 2 cm, i.e. closest to the free surface.

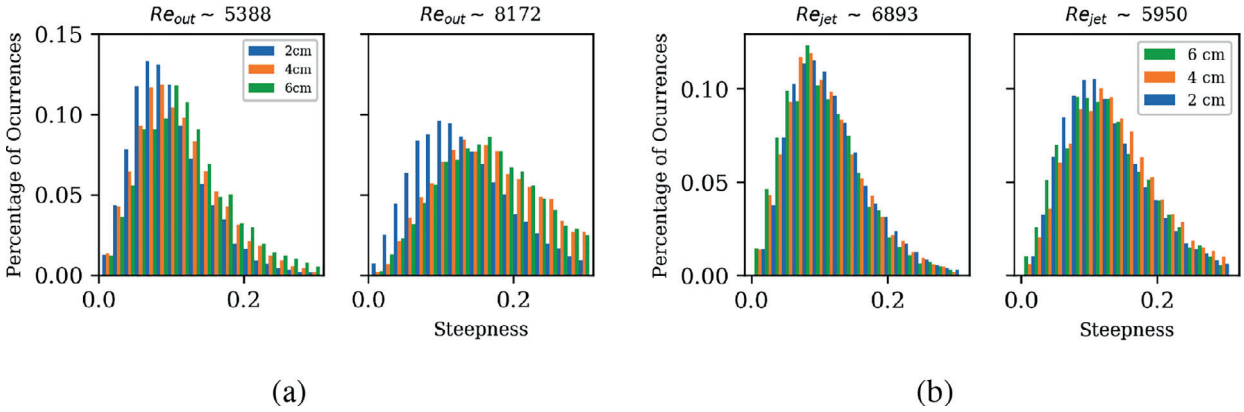

Fig. 7. (a) Wave steepness distribution for similar Re_{out} in the different l. (b) Wave steepness distribution for similar Re_{jet} and Fr in different l. (For interpretation of the references to color in this figure legend, the reader is referred to the web version of this article.)

outlet (labeled "top" in figure) have a different steepness distribution than the waves observed in the second half or closer to the free surface (labeled "bottom"in the figure). In particular, all the cases have a shift on the peak of the distribution (mean steepness) of at least 0.04. Also, there is an increase of waves with larger steepness even beyond the maximum of the first (bottom) distribution. This shows that disturbances that were formed closer to the outlet had mean steepness smaller than the disturbances present further down on the jet. Together with the findings in Fig. 5 a, this shows that the $\lambda_{jet} \leq \lambda_{out}$, i. e. the wavelength stays the same or decreases.

Fig. 7 shows the steepness distributions in 2 different similitude cases: when considering the Reynolds number at the tube exit (Fig. 7 a) and when considering the Reynolds number at the confluence point (Fig. 7 a). In Fig. 7 a there is a change in the steepness of the disturbances for similar values of Re_{out}, over the different l used. This could be interpreted as a confirmation of a proportionality between ak and x, the vertical position of the disturbance in the jet. The distributions exhibit a change in the mode and a higher percentage of occurrences for steeper waves when l increases. However, the distributions for $l = 4$ cm and $l = 6$ cm have closest values compared to the distribution for $l = 2$ cm. This can be related to the findings in Fig. 5 a where a change in the characteristic λ can be inferred from the data. If instead Re_{jet} is considered (Fig. 7 b), the distributions for the different distances are similar for all the cases. This means that when the falling jet has developed the same Re_{jet} the waves will have a similar steepness distribution independently of the total height they have fallen. The Reynolds similitude tells us about the turbulence level in the jet, which could be an indication that the level of turbulence in the jet is related to the instabilities presented in the surface of the jet. As far as the knowledge of the authors goes, this result has not been presented in another paper for the case of a falling jet.

The number of bubbles per image was estimated for each experimental test case. The mean number per image is an important quantity as it shows the permanency of the bubbles in the plume. It is visible in Fig. 8 a that the number of bubbles increases with the Reynolds number for the different jet lengths l. When comparing the results for different l, it is visible that the mean increases with l after a certain Re_{jet}, for all cases. We recall that for $l = 6$ cm there was a decrease in steepness between $Re_{\text{jet}} = 7000 - 8000$ compared to $l = 4$ cm, cf. Fig. 5 b. These results combined support the hypothesis that the wave steepness is an important parameter in air entrainment.

As discussed in Section 2, a new definition of the onset velocity was needed to fit the conditions of this experiment. After careful consideration of the experiment results and literature findings, the onset velocity was defined as the velocity for which the mean number of entrapped bubbles across the measurement time is 3. The estimate is a result of the findings presented on Fig. 8 a, where we see a jump after this threshold and the bubble count follows a linear trend with Re_{jet}. The onset velocity was

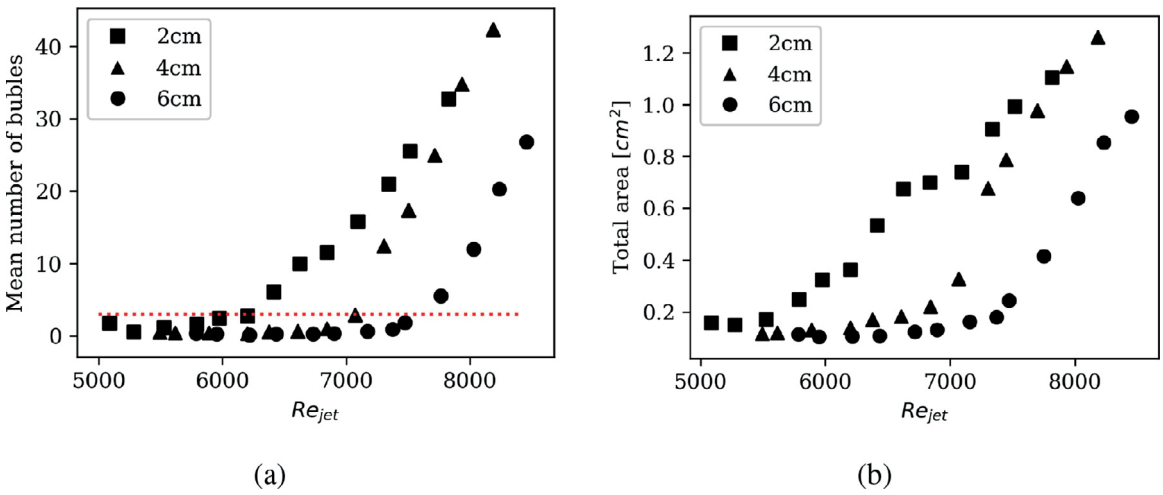

Fig. 8. Mean number of bubbles per image (a) and area occupied by bubbles in the FOV (b), both compared with the Reynolds number at the confluence point Re_{jet}. The dotted line in (a) shows the threshold of entrainment where the mean number of bubbles is $N = 3$.

measured to be 1.2 m/s, which is comparable to the velocities found in Wang et al. (2016), Chanson et al. (2006), Harby et al. (2014), Qu et al. (2013).

An estimation of the total area of air entrained was also performed by adding the visible area occupied by bubbles in a single image. While here only a single camera position was used, it appears reasonable that the phenomenon/statistics show (some degree of) rotational symmetry. However, our setup did not allow for direct experimental verification of the assumption.

The air area expresses the amount of aeration produced in the process. Moreover, it can also explain the difference in the bubble counts, as we can expect larger bubbles in the higher Reynolds flows. In Fig. 8 b it is shown that the area of entrained air grows with the Reynolds number also. However, air volumes for $l = 2, 4$ cm are higher than those for $l = 6$ cm. Nonetheless, it is possible that the results for $l = 6$ cm are biased by two factors: overlapping and bubble size threshold. The case of $l = 6$ cm is the only case where overlapping of the bubbles is present. Despite this, the proportion of time where the bubbles are overlapping seems to give an under estimate of only 5% in the worst case. This is because the bubbles tend to move downwards due to the flow and there is only a small number of frames with overlapping. A more significant source of bias could be the difficulty to distinguish a bubble from a bulk of water; in order to approximate an elliptic contour, a size threshold is needed. We consider here that contours need to have at least 6 pixels in area and maximum axis size of 120 pixels. This translates to a limit of 4mm for a length of any ellipse axis. Due to this limitation a contour will not be found if a larger bulge of water is encountered. Furthermore, the image consists in a mix between smaller bubbles and bulks of water and only the small bubbles will be accounted for thus resulting in under estimation of the entrained air.

From Figs. 8 and 5 b, it is noticeable that even with similar steepness for similar Re_{jet}, there is a difference in the entrainment conditions for the different jet lengths. So far, the parameters considered to find an entrainment condition were the forces and velocities of the jet and characteristics of the disturbances. However, we have also shown that the jet characteristics (wavelength and amplitude) changed with the jet length, (cf. Figs. 3 and 5 a). It is therefore, intuitive to consider a parameter to account for the effects of the jet dimensions. To this end, we considered the wave-jet ratio defined as

$$\frac{ak}{L_D}, \quad \text{with} \quad L_D = 1 - \frac{D_{\text{jet}}}{l}. \tag{8}$$

The wave-jet ratio gives an idea on how steep are the disturbances when compared to jet dimensions and together with the Reynolds number can help to understand the present phenomenon. As shown in Fig. 9 a, the number of bubbles generated seems to be dependent on the steepness of the present disturbances. Using the previously defined onset criterion of 3 bubbles (shown in the figure with the dashed line), the data after the onset follows a linear trend. Moreover, when using our wave-jet ratio the entrainment condition had a similar value for all the data independently of the jet length. A similar behaviour is observed with the area of entrained air. This area can be estimated with the area fraction, which is the ratio of air area over total area of the FOV (Fig. 9 b). The equivalent entrainment onset condition requires that 0.06 of the area fraction is occupied by air. After this threshold, the remaining data follows also a linear trend. A related interesting finding is that the steepness needed to create entrainment increases with the length of the jet. Thus, the onset condition of entrainment is dependent on the dimensions of both the jet and the disturbances. For a longer jet a larger steepness seems to be required to obtain the possibility of entrainment.

For the longest jet length $l = 6$ cm we would expect a larger amount of bubbles created. However Fig. 9 a shows that the longer jet produces less bubbles. This could be related to the size of the air pockets created by the different jet lengths which are bigger for the longer jet. These pockets are not accounted for in the image processing when they have larger diameters than the threshold. This underestimation is visible also in the area fraction (Fig. 9 b) where we would expect to see a larger proportion of air entrained compared to the total image area. In contrast, it is interesting to notice that the mean radius of the generated bubbles decreases with the velocity of the jet, moreover, the decrease is proportional to the change in wavelength in the disturbances, as shown in Fig. 10. Although for the results in $l = 6$ cm the radius of the bubbles is more a consequence of the breakup of big air pockets into smaller ones due to the instabilities of the surface tension compared with the inertia of the jet. Similar trends were found by Oguz (1998) with the wavelengths and the maximum bubble radius. Nonetheless, the results of this study are difficult to compare with Oguz (1998) because of the different orders of magnitude. In addition, the bubbles in the mentioned study are mostly spherical, while in our case they are mostly ellipsoidal.

For a particular jet length, the influence of the disturbances on the air entrainment can be summarized with the steepness of the disturbances. But the main finding is the relation between the

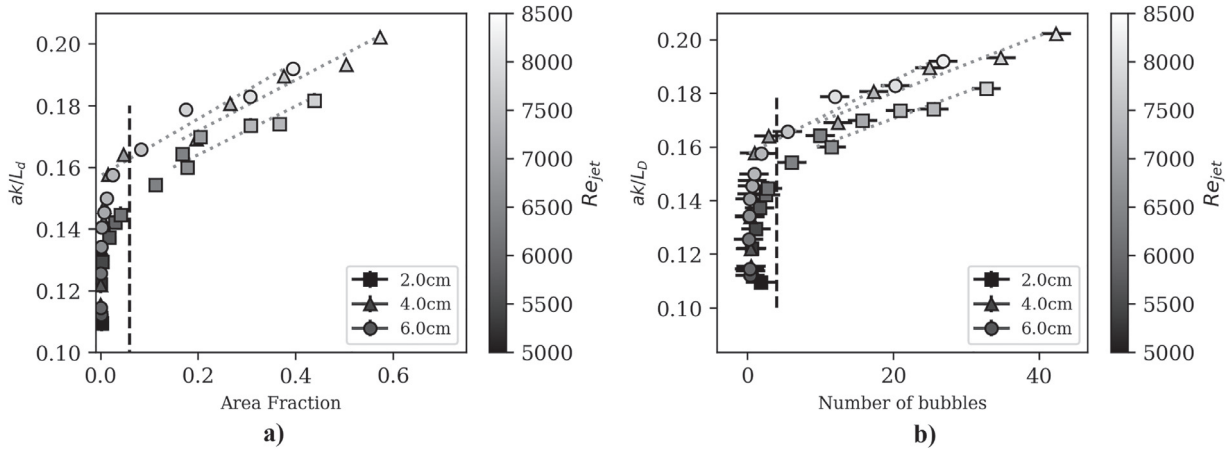

Fig. 9. (a)Wave-jet ratio as defined in Eq. (8) against mean number of bubbles. (b)Wave-jet ratio against area fraction. The black dashed line represents the entrainment condition from which we consider the onset of air entrainment. Linear fits for the jet-disturbance ratio against bubble count and void fraction are presented with colored lines. Only data points with air entrainment were considered.

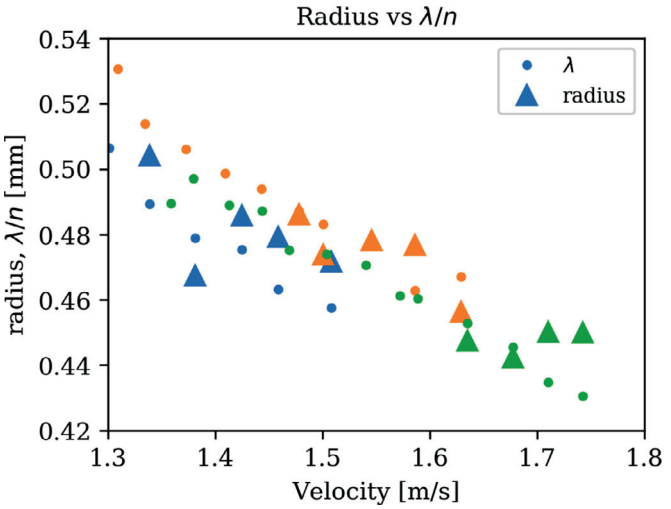

Fig. 10. Mean bubble radius and λ/n for the jet dusturbances as a function of the mean jet velocity. For each falling length $l = 2, 4, 6$ cm, we have different $n = 12, 16, 19$. As through out the paper, $l = 2$cm is blue, $l = 4$cm is orange and $l = 6$cm is green. (For interpretation of the references to color in this figure legend, the reader is referred to the web version of this article.)

wave-jet ratio and the entrainment onset as shown in the joint results graphs (Fig. 9 a,b).

From the analysis of the jet, it is evident that the development of the surface is influenced by the growth of the boundary layer inside the tube which is defined by the jet velocity. Nonetheless, the influence of the sharp tube exit and the ratio L_c are important factors for the development of the jet after exiting the tube. Therefore, a careful examination of the generated disturbances is necessary when looking into the details of the air entrainment. Perhaps considering statistical analysis is more significant for the overall phenomena, specially when considering longer time periods. The results of the present research confirm that in this regime, the disturbances that hit the water surface are the basic mechanism from where air entrainment occurs. In previous work Zhu et al. (2000) and Ohl et al. (2000) it has been suggested that the front of the wave is responsible for generating the air cavity thanks to the stagnation pressure. Using steepness as a parameter to quantify the front of the wave can help to understand the amount of pressure created and therefore relate to the entrainment.

It is interesting to also notice that the dimensions of the jet can generate important changes in the air entrainment conditions. When increasing the falling distance, it can be inferred that there will be an increase in the amount of entrainment. With these experiments, we found out that it is not necessarily increasing but limited by the length of the jet, which will determine the main frequencies and, through the dispersion relation, determine the wavelengths. Therefore, even if there is an overall increase in the amplitude with the falling distance, the main frequencies are dependant on the length scales of the problem. This result suggests that quantifying the steepness of the disturbances could result in prediction of entrainment parameters when comparing to the jet dimensions.

5. Conclusion

Air entrainment by a circular falling jet was investigated for a range of flow velocities and falling distances. Careful measurements of the jet disturbances and bubble plumes were made by means of image processing. A relation between the theoretical boundary layer thickness $\bar{L}$ and the wavelength of the disturbances was found, supporting the idea that the boundary layer perturbations give rise to the disturbances at the surface of the jet. Moreover a relation between the steepness distribution and the Reynolds number developed by the jet was found. This result may suggest that the turbulence level in the jet continues to affect the development of the surface disturbances during the fall.

The definition of a new entrainment onset condition was inferred from the experimental results, which in this case was set at a jet velocity of 1.2 m per second, corresponding to a temporal mean of at least three bubbles per image throughout the experiment. After the onset condition, air entrainment is persistent through the length of the experiment. For the jet disturbances, the use of the steepness as main non-dimensional parameter proved to give a good quantitative relation. The mean values of steepness and bubble count showed a linear relation for each jet length considered. Moreover the ratio between disturbance dimensions and jet dimensions give a clear trend of the entrainment condition. We also found that for our particular tube, the ratio at entrainment is defined by $ak/L_d \sim 0.15$. Using this ratio, all the data follows a similar linear trend. Also a relation between the wavelength of the disturbances and the mean bubble radius is found, which strengthens the hypothesis that disturbances influence the air entrainment.

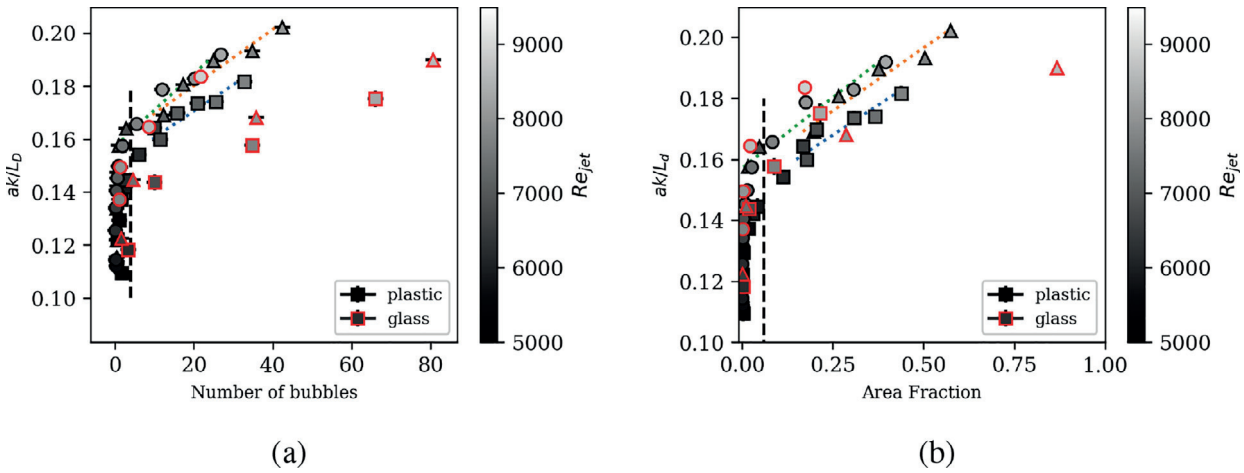

Fig. A1. (a)Wave-jet ratio as defined in Eq. (8) against mean number of bubbles. (b)Wave-jet ratio against area fraction. Data with red edges correspond to glass tube. Marker shape represents the falling distance as in previous graphs: squares for $l = 2$ cm, triangles for $l = 4$ cm and circles for $l = 6$ cm. The black dashed line represents the entrainment condition from which we consider the onset of air entrainment. (For interpretation of the references to color in this figure legend, the reader is referred to the web version of this article.)

Declaration of Competing Interest

The authors declare that they have no known competing financial interests or personal relationships that could have appeared to influence the work reported in this paper.

CRediT authorship contribution statement

R.G. Ramirez de la Torre: Conceptualization, Data curation, Resources, Writing - review & editing, Methodology, Software, Validation, Formal analysis, Writing - original draft. **Miroslav Kuchta:** Conceptualization, Resources, Writing - review & editing, Software. **Atle Jensen:** Conceptualization, Resources, Writing - review & editing, Methodology, Supervision, Project administration, Funding acquisition.

Acknowledgements

Funding from the Norwegian Research Council through the project 'Rigspray' (grant number 256435) is gratefully acknowledged. The authors will like to acknowledge Geir K. Pedersen and Arne Bøckman of their input in the manuscript. The authors will also like to acknowledge Olav Gundersen for the help in the experimental setup.

Appendix A. On the wettability of the exit material

The experiments in the main body of the text were conducted with a plastic tube. Here, we shall briefly investigate the role of the material. To this end, we repeat our experiments with the previous experimental setup modified by replacing the exit tube with a glass one of the same dimensions. The different material will change the wettability, which has an influence on the boundary layer thickness and the generation of turbulence. Nonetheless, after reviewing the literature available (Kiger and Duncan, 2012; Bińi, 1993; Eggers and Villermaux, 2008; Law and Zhao, 2016) it is not clear how the wettability of the exit material will influence the development of the jet and its surface disturbances. Moreover, it is not clear whether/how the material effects the air entrainment.

Fig. A.11 shows both the number of bubbles and the area fraction results for both tube materials. It is visible that there is a consistent bending point where the entrainment condition can be established independently of the material used. It is clear from the figure that after the onset the remaining data shows a linear trend for both materials. For the glass results, there is an increase in the Reynolds numbers because the diameter of the falling jet increases due to wettability.

For the number of bubbles (Fig. A1 a), the data for glass in $l = 6$ cm has the same trend as the plastic data, with the same wave-jet ratio value for the entrainment condition and similar slope. However, the data for $l = 2, 4$ cm shows a different slope. In contrast, the area fraction (Fig. A1 b) seems to have a similar trend in all cases for both materials. Independently of the material, the data for $l = 4$ cm has the highest number of bubbles and the highest area fractions. The possible reasons for this behavior can be the size of the air pockets created by the different jet lengths which are possibly dismissed in the image processing according to the threshold. Additional contributions can come from the breakup of big air pockets into smaller ones due to the instabilities on the bubble surface. These reasons were detailed further in the Discussion.

We believe that the difference in the results between tubes with different material is due to wettability. Even though the materials used in this experiment have not been measured for wettability, the reported data in the literature shows a difference for non-treated glass and acrylic plastic (Law and Zhao, 2016; Sumner et al., 2004; Rymuszka et al., 2014; Samuel et al., 2011).

These additional results show that the our experiment is reproducible independently of the tube material. Further studies can be done to find the relation between the tube material and its effect on the entrainment.

Supplementary material

Supplementary material associated with this article can be found, in the online version, at 10.1016/j.ijmultiphaseflow.2020.103424

References

Bin, A., 1988. Gas entrainment by plunging liquid jets. Forsch. Ingenieurwes. 54 (4). 136–136
Bińi, A.K., 1993. Gas entrainment by plunging liquid jets. Chem. Eng. Sci. 48 (21), 3585–3630.
Chanson, H., Aoki, S., Hoque, A., 2006. Bubble entrainment and dispersion in plunging jet flows: freshwater vs. seawater. J. Coastal Res. 664–677.
Cummings, P.D., Chanson, H., 1999. An experimental study of individual air bubble entrainment at a planar plunging jet. Chem. Eng. Res. Des. 77 (A2), 159–164.
Dai, Z., Hsiang, L., Faeth, G., 1997. Spray formation at the free surface of turbulent bow sheets. In: Proceedings of the 21st ONR Symp. on Naval Hydrodynamics, pp. 490–505.

Davoust, L., Achard, J., El Hammoumi, M., 2002. Air entrainment by a plunging jet: the dynamical roughness concept and its estimation by a light absorption technique. Int. J. Multiphase Flow 28 (9), 1541–1564.
Deane, G.B., 1997. Sound generation and air entrainment by breaking waves in the surf zone. J. Acoust. Soc. Am. 102 (5), 2671–2689.
Eggers, J., Villermaux, E., 2008. Physics of liquid jets. Rep. Prog. Phys. 71 (3), 036601.
El Hammoumi, M., Achard, J., Davoust, L., 2002. Measurements of air entrainment by vertical plunging liquid jets. Exp. Fluids 32 (6), 624–638.
Harby, K., Chiva, S., Muñoz-Cobo, J.-L., 2014. An experimental study on bubble entrainment and flow characteristics of vertical plunging water jets. Exp. Therm Fluid Sci. 57, 207–220.
Jiang, X., Zheng, G., Pei, Y., 2008. A new probability distribution function of wave steepness. J. Ocean Univ. China 7 (3), 246–250.
Kiger, K.T., Duncan, J.H., 2012. Air-entrainment mechanisms in plunging jets and breaking waves. Annu. Rev. Fluid Mech. 44, 563–596.
Kusabiraki, D., Yamagiwa, K., Yasuda, M., Ohkawa, A., 1992. Gas entrainment behavior of vertical plunging liquid jets in terms of changes in jet surface length. Can. J. Chem. Eng. 70 (1), 181–184.
Lamb, H., 1993. Hydrodynamics. Cambridge university press.
Law, K.-Y., Zhao, H., 2016. Surface Wetting: Characterization, Contact Angle, and Fundamentals. Springer Switzerland.
Lin, S., Reitz, R., 1998. Drop and spray formation from a liquid jet. Annu. Rev. Fluid Mech. 30 (1), 85–105.
McKeogh, E., Ervine, D., 1981. Air entrainment rate and diffusion pattern of plunging liquid jets. Chem. Eng. Sci. 36 (7), 1161–1172.
Oguz, H.N., 1998. The role of surface disturbances in the entrainment of bubbles by a liquid jet. J. Fluid Mech. 372, 189–212.
Ohl, C., Oguz, H., Prosperetti, A., 2000. Mechanism of air entrainment by a disturbed liquid jet. Phys. Fluids 12 (7), 1710–1714.
Qu, X., Goharzadeh, A., Khezzar, L., Molki, A., 2013. Experimental characterization of air-entrainment in a plunging jet. Exp. Therm. Fluid Sci. 44, 51–61.
Reed, H.L., Saric, W.S., Arnal, D., 1996. Linear stability theory applied to boundary layers. Annu. Rev. Fluid Mech. 28 (1), 389–428.
Rymuszka, D., Terpiłowski, K., Hołysz, L., 2014. Influence of volume drop on surface free energy of glass. Annales UMCS, Chemia 68 (1–2), 121–132.
Samuel, B., Zhao, H., Law, K.-Y., 2011. Study of wetting and adhesion interactions between water and various polymer and superhydrophobic surfaces. J. Phys. Chem. C 115 (30), 14852–14861.
Sumner, A.L., Menke, E.J., Dubowski, Y., Newberg, J.T., Penner, R.M., Hemminger, J.C., Wingen, L.M., Brauers, T., Finlayson-Pitts, B.J., 2004. The nature of water on surfaces of laboratory systems and implications for heterogeneous chemistry in the troposphere. PCCP 6 (3), 604–613.
Tayfun, M.A., 2006. Distributions of wave steepness and surf parameter. J. Waterway Port Coastal Ocean Eng. 132 (1), 1–9.
Veron, F., 2015. Ocean spray. Annu. Rev. Fluid Mech. 47, 507–538.
Wang, H., Bertola, N., Chanson, H., 2016. Bubble entrainment in vertical plunging jets. In: Proceedings of the Australasian Fluid Mechanics Conference. Australasian Fluid Mechanics Society, pp. 459–461.
Zhu, Y., OĞUZ, H.N., Prosperetti, A., 2000. On the mechanism of air entrainment by liquid jets at a free surface. J. Fluid Mech. 404, 151–177.

Paper II

3D Particle Tracking Velocimetry applied to bubble plumes from a free falling jet

Reyna Guadalupe Ramírez de la Torre, Miroslav Kuchta, Atle Jensen

Available in Proceedings of the 13th International Symposium on Particle Image Velocimetry – ISPIV 2019.

II

13th International Symposium on Particle Image Velocimetry – ISPIV 2019
Munich, Germany, July 22-24, 2019

3D Particle Tracking Velocimetry applied to bubble plumes from a free falling jet

R.G. Ramirez de la Torre[1*], Miroslav Kuchta[2], Atle Jensen[1]

[1] University of Oslo, Department of Mathematics, Oslo, Norway

[2] Simula Research Laboratory, Fornebu, Norway

[*] reynar@math.uio.no

Abstract

The focus of the present study was the behaviour of a bubble plume created by a circular free falling jet. The objective was to find a relation between the disturbances on the jet surface and the air entrainment process. To achieve this, the instabilities of the free falling jet were characterized and compared with the size distribution and generation rate of the bubbles created in the plume.The bubble trajectories were obtained and used to determine the jet-pool interaction after the impact.

1 Introduction

In the atmosphere and within the marine boundary layer the interaction between air and water is constant and takes different forms. In the case of the phenomena involving droplets or bubbles, there is a large number of challenges: the three-dimensionality of the phenomena, the highly turbulent regions, the wide distributions of sizes in both droplets and bubbles, to name but a few. An important example of this difficult phenomena is ocean spray in artic sea freezing on top of vessels. Understanding of this phenomenon is important for the safety of installations, ships and people that operate in the Arctic environment. The icing phenomena and its consequences have been documented for several years (see e.g. Ryerson (2013)). Some references report that the major causes of icing are the sea spray and the atmospheric conditions (Bodaghkhani et al., 2016). The sea spray formation is caused by wave impact and wind. According to Borisenkov and Pchelko (1975) more than 90% of the icing is caused by the spray that comes from wave impact. It has been reported that the physical behaviour of wave impact is not properly understood. Furthermore, the multi-scale nature, complexity of spray and icing require that the research on this field is separated into smaller problems, such as the modelling of the free-surface, wave slamming, air entrainment during the impact, water sheet and jet formation during the wave slamming, water sheet and droplet breaking caused by wind and droplet trajectories before they impact on the surface of ships or structures (Bodaghkhani et al., 2016; Dommermuth et al., 2007).

The ambition of spray and icing research is to generate models that are able to predict the amount of icing on a structure from ocean spray. Here, we focused on experiments to bring understanding of the spray and bubble plume phenomena, in particular, the size distributions, which are not well known and are an important input for simulations of breaking waves on naval structures. A simplified system, which however, is still complex enough to capture the difficulty of measuring sea spray and air entrainment is the circular falling jet. For the case of bubble generation in falling jets, the ratio of entrained air and the size distribution of the bubbles has been estimated using conductivity probes, resistivity probes and acoustic probes (Chanson et al., 2006; Wang et al., 2016; Deane, 1997; Kolaini, 1998). All of these probes have been used with positive outcomes but the characteristics of the observed phenomena also show the limitations of the applied techniques. These probes are invasive methods and the data obtained is only for a particular point in the domain. For highly turbulent flows these techniques are non-adequate, except maybe the acoustic probes. Moreover, the resistivity and conductivity probes are dependent on the size of the instrumentation, i.e. different probe sizes can give different measurements for the same parameters on the jet (Chanson et al., 2006). This is not the case for the acoustic probes, nonetheless these types of probes can only approximate the void fraction and not the size distribution.

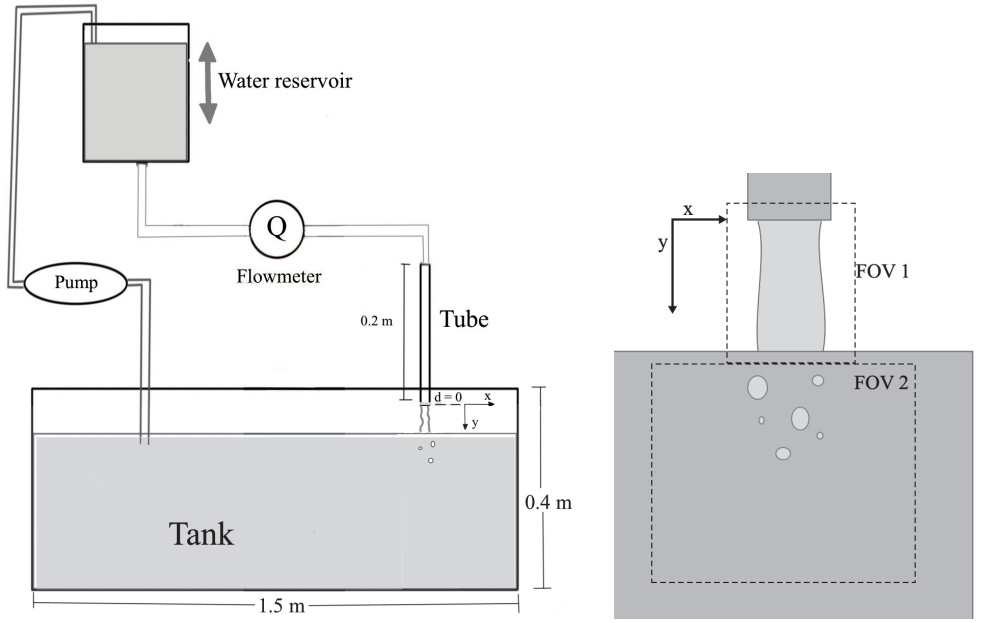

(a) Diagram of full experimental setup. (b) Different fields of view for analysis.

Figure 1: Experimental Setup.

Imaging methods can in some cases be used for measuring droplets and bubbles. By using images, it is possible to capture the complete domain, in contrast to the point-wise measurements obtained by the probes. Post processing of these images is commonly done with Particle Image Velocimetry (PIV) or Particle Tracking Velocimetry (PTV). The usage of one of these algorithms is determined by the type of analysis that is desired. PIV measurements are commonly used to track the fluid movements from an Eulerian approach, PTV measurements are used to obtain a Lagrangian description. For PTV, using more than one camera at the same time can result in 3D reconstruction of the trajectories of the particles and their velocities. The advantage of this kind of algorithms is that they consider the camera parameters to estimate the positions of the blurry particles present in the images and with the correlation of the images from the different cameras, reduce the error on the positions for each particle in each time step.

In this work imaging techniques and a 3D-PTV algorithm were used to understand the parameters involved in the air entrainment produced by a circular falling jet. The experiments involved the study of different parts of the process: formation and development of disturbances in the surface of the jet, identification of the conditions under which the entrainment occurs and finally the formation of bubbles and its characteristics. The experimental setup and the different approaches and measuring techniques needed to understand each part are described in section 2. We present and analyze the obtained results in section 3. Conclusions are drawn in section 4.

2 Experimental Description

The experiments were conducted in a small tank with dimensions 1.50 m $\times$ 0.40 m $\times$ 0.40 m, as shown in Figure 1. Water was stored in a 10 litre reservoir, then went down through a hose towards the tank. In the middle of its path, there was a flowmeter, from which the flux or flow rate (Q) was obtained. Before falling down to the tank, the water went through the exit pipe, which was a 20 cm long plastic tube. The tube was fixed such as to ensure a perpendicular fall of the jet. To create the different falling speeds, the reservoir was moved in the vertical direction. The water was also recycled with the help of a pump. The pump was off during the measurements to avoid undesired effects.

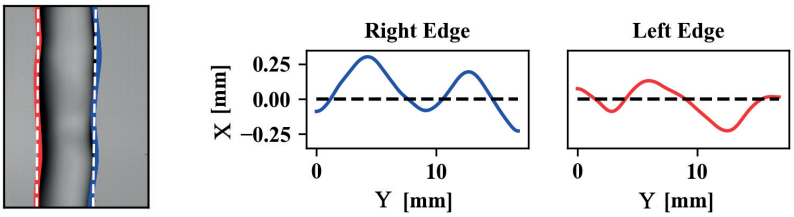

(a) Jet image and edge detection, the dashed white line represents the zero crossing.

(b) Graphs of edges in data shape.

Figure 2: Edge extraction process.

2.1 Jet disturbances and the entrainment process

For the jet disturbances, the images were obtained with a Photron FASTCAM SA5 camera. The frame rate was 500 FPS with $1/2000$ ms of shutter speed. The image resolution was 640×1024 pixels. The Field of View (FOV) was approximately 2 cm height, see Figure 1(b). The illumination was provided by LED lamps. The light was diffused with white plastic sheets and difusser sheets. As the disturbances presented in the surface were non-controlled, it was expected for them to have random behaviour. Therefore, careful record of the amplitude a, wavelength λ, and frequency f of the disturbances was made and the jet disturbances were analyzed as surface waves. As shown in Figure 2, the edges of the jet were extracted from the images and collected in a space-temporal array: $x(y,t)$. A mean level was defined by averaging the data set in time $\xi(y) = \overline{x(y,t)}$. Then, the wave height was obtained by subtracting the mean level: $\eta(x,t) = x(y,t) - \xi(y)$. A wavelength ($\lambda$) in η was define as the length from through to trough and the amplitude (a) of the wave was defined as the height of the crest between the throughs.

For each falling distance d we had a range of Q's. For each Q, we obtained an outlet velocity (V_{out}) and estimated a falling velocity at the confluence point (V_{jet}) with the equations

$$V_{jet} = \sqrt{V_{out}^2 + 2gd}, \quad V_{out} = \frac{Q}{A}, \tag{1}$$

where A is the cross section area of the tube and g is gravity acceleration. From these velocities we also obtained Reynolds numbers for the outlet flux (Re_{out}) and estimated a Reynolds number for the falling jet (Re_{jet}). In general, the Reynolds number is defined as

$$Re = \frac{VD}{\nu}, \tag{2}$$

where D is the diameter of the correspondent flow, for Re_{out}, $D = D_{out}$, the diameter of the tube and for Re_{jet}, $D = D_{jet}$,the diameter of jet at the confluence point, and ν is the dynamic viscosity of water.

For the entrainment process, a set up of synchronized cameras was used to capture simultaneous images of the jet and the entrainment underwater. Two AOS Promon U1000Mono cameras were used. These cameras were synchronized at 500 FPS, with 1/500 ms shutter, with resolution 608×800 pixels. Both FOV's were around 2-3cm height. The FOV of the first camera was centered at the jet falling while the other camera's FOV was centered in the confluence area under the pool surface.The recordings were 20 seconds long. The illumination was provided in the same way as in the previous case. These synchronized image sequences had as main objective the visualisation of the entrainment process in a qualitative way. Also, the underwater images were used to obtain a number of produced bubbles for each Q and each d.

2.2 Bubbles characteristics

For the tracking of bubbles, a group of 4 AOS Promon U1000Mono cameras was used. The cameras were synchronised with a frame rate of 350 FPS, 1/500 ms shutter and an image resolution of 1280×720 pixels.

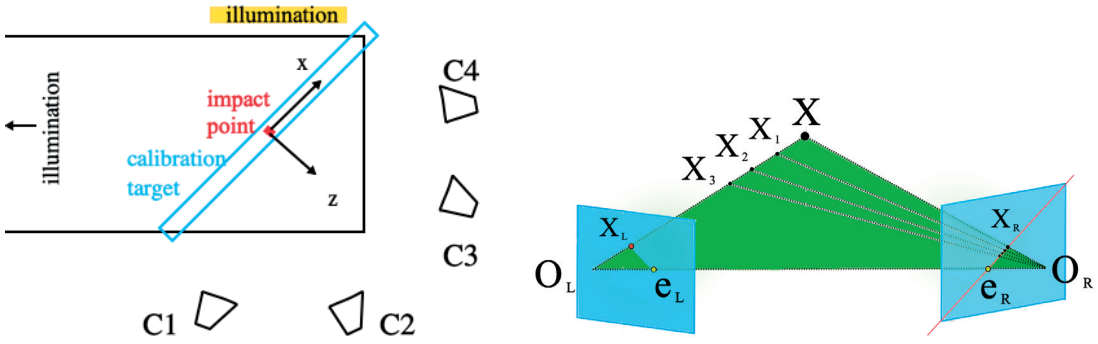

(a) Diagram of the cameras setup for 3D PTV. C1-C4 shows the position of the cameras compared to the tank. The diagram shows also the calibration target in blue. The outlet of the tube to the surface of the water is pinpointed with the red dot.

(b) Diagram of algorithm to reconstruct 3D trajectories with epipolar lines. Points $O_L$and O_R represent the centers of each camera lens, while X represents an arbitrary particle. X_L and X_R are the projections of X in the respective image plane. Each camera center is also visible in each others image plane. These so called epipolar points are depicted by points e_L and e_R. The line $\overline{O_L X}$ is seen as a point in the left camera, whereas the same line is seen as an epipolar line $\overline{e_R X_R}$ in the image plane of right camera. The same applies to line $O_R X$ which is seen as a point in the right camera and as an epipolar line in the left camera's image plane (Maas et al., 1993).

Figure 3: PTV Camera setup and description of the 3D position algorithm.

The illumination was provided by a similar setup as in the previous cases. The cameras were arranged in a stereoscopic setup for the reconstruction of the 3D positions of the bubbles, cf. Figure 3(b). The FOV is approximately 12 cm height and is below the area of analysis used in the previous setups where the plume is totally developed. OpenPTV software was used to reconstruct the 3D positions and trajectories of the bubbles. OpenPTV uses image processing to detect particles in the images. Then using the method described in Maas et al. (1993), finds the correspondences in the 4 images, in this way the three dimensional positions are reconstructed for each time step.

PTV method represents the Lagrangian approach to investigate flows. To obtain three dimensional trajectories, the particles need to be matched among all views. The method used by OpenPTV finds correspondences based on epipolar geometry. Figure 3(b) depicts the definition of an epipolar line with two cameras. Since the line $\overline{O_L X}$ passes through the optical center of lens O_L, the respective epipolar line in the right image must pass through the epipolar point regardless of where point X is located. In OpenPTV the relative position of the cameras system are known from a previous and very careful calibration. When a particle is observed in one image, the same particle has to be observed on a known epipolar line in the other image. Furthermore, if points X_L and X_R are known, their projection lines $\overline{O_L X}$ and $\overline{O_R X}$ are also known. Consequently, point X is located exactly at the intersection of the two projection lines and thus can be calculated from the image coordinates of the two images. This figure illustrates the need for a good calibration for three-dimensional particle tracking.

The next processing stage is to compare particles in consecutive time steps and determine their trajectories. The length of the trajectories is dependant on the position, the size and the acceleration of the particle. Tracking can be especially difficult with a large number of particles present. According to Malik et al. (1993) the particle spacing displacement ratio p is a fundamental indicator on the difficulty to track particles with this method. The ratio is defined as

$$p = \frac{\Delta O}{u \Delta t} \tag{3}$$

with ΔO the mean particle spacing, u the mean velocity of the particles and Δt the time step between images. For $p > 1$ tracking is reliable, while for $p < 1$ tracking becomes difficult. In other words, the farther particles are from each other and the slower they move, the more reliable the method is. OpenPTV uses a spatio-temporal tracking algorithm which is described in Maas et al. (1993) and Willneff (2003). As input, this algorithm needs eight parameters. These include the minimum and maximum displacement in each coordinate direction, the angle of the particle in the direction along its trajectory and a magnitude

$d[m]$	Re	We
0.02	6100-9000	1-137
0.04	7200-9700	9-155
0.06	8100-10400	5-158

Table 1: Relevant nondimensional parameters for each falling distance d

of acceleration. Since these parameters constitute the boundary conditions of the particle velocities, it is important to have an estimate of the expected velocities. After obtaining the correspondences and the trajectories, custom made Python codes were used to analyze the data obtained, plot the trajectories and obtain the velocity fields.

A range of Weber number (We) can be obtained from the bubble size distribution. We was defined as

$$We = \frac{\rho V_{jet}^2 D_b}{\sigma}, \tag{4}$$

where ρ is water density, D_b is the bubble diameter and σ is the surface tension for air and water. Weber number is an important parameter on the interaction of the bubble with the media. It expresses the ratio between the inertial forces and the surface tension and it is the relevant parameter to describe the deformation of the bubbles. Therefore is important to describe their possible trajectory and the coalesence probability. For bubbles that present low deformation, Weber number has values of $O(2)$ (Legendre et al., 2012). If we consider the bubbles to be spheroids, with axes a and b, $We > 10$ would signify a ratio $a/b > 4$. Reynolds and Weber number for the different experiments made can be found in Table 1.

3 Results

The air entrainment process has been studied in numerous works and for different geometries (Kiger and Duncan, 2012; Zhu et al., 2000). The conditions of its development have been shown to be dependant on a large number of parameters. Therefore it keeps being interesting to find the different dependencies of this problem. In this study, the focus was to understand the formation of air pockets due to the disturbances that appear on the surface of a circular falling jet and the dynamics of the bubble plume formed after the air entrainment. We shall next describe the most important findings.

3.1 Jet disturbances and entrainment process

A great amount of work has been done to understand the air entrainment process (Kiger and Duncan, 2012; Zhu et al., 2000; Soh et al., 2005; Chanson et al., 2004), the synchronised surface-underwater images are qualitative evidence of the conditions of the phenomena. In Figure 4 it is possible to follow the impingement of two different disturbances in to the pool. The main difference between these disturbances is that the first (closest to the pool, Fig.4(a)) has longer wavelength compared to the second. In other words, the first disturbance has smaller steepness than the second one. It is clear that the first disturbance impinges the pool and enters without the generation of any air pocket or any significant change in the pool surface (Fig. 4(a)-4(c)). Subsequently, the second disturbance approaches the pool surface and impinges on it. After the impingement an air pocket is created and it is pulled down by the jet velocity (Fig. 4(d)-4(g)). The finger finally breaks to form a bubble that will continue travelling underwater pulled by the jet. This is a clear example of a typical entrainment occurrence in the experiments developed for this study. The image sequence is comparable to the sketches presented in Kiger and Duncan (2012) and Zhu et al. (2000) for disturbances with large amplitude. In this study we put forward a hypothesis that the steepness of the disturbance is possibly more significant than the amplitude. This hypothesis can be supported by Figure 4, where two disturbances with comparable amplitude produced different effects on the pool and the disturbance with considerably smaller wavelength was the only one that produced entrainment. This possible dependency should be further studied.

In addition to the raw entrainment of air in to the pool, it is also interesting to turn our eyes to the formation of bubbles after the air pockets broke. For the different d there is a different span of Reynolds

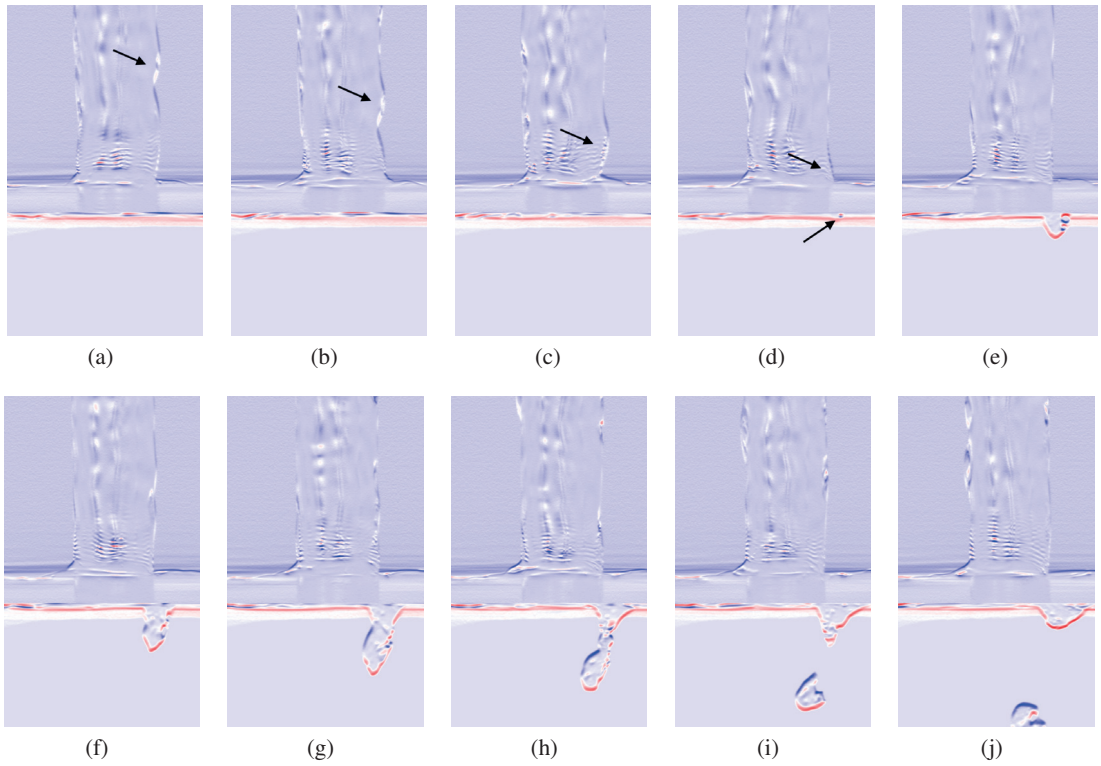

Figure 4: Sequence of images that shows the entrainment process for a steep disturbance in the jet. The diameter of the jet at the impingement point is approximately 5mm. Sobel derivatives were used to enhance the edges of the interfaces. (a) Two waves are visible, the top one with larger steepness (pointed with the arrow), this is the wave to follow. (b) The first wave enters, there is no air entrainment. (c) The second wave approaches. (d) The second wave enters the pool, air entrainment begins. (e) The formation of the air finger is visible while the jet pulls it down. (f) The air finger grows. (g) The air finger continues growing. (h) The finger break up starts caused by the speed of the jet. (i) The finger finally breaks and a bubble is created. (j) The cavity from the finger closes and the surface starts contracting upwards again.

numbers that we showed in Table 1. From the results of the experiments, it is possible to say that the air entrainment has a Reynolds onset value close to 8000. These results are summarized in Figure 5. Although for large d it is also noticeable that the number of bubbles is reduced. This can actually be explained by inspecting the images of the entrainment. The air pockets produced by greater Reynolds are also larger in size which reduces the count of bubbles. The bubbles visible in this setup will have greater size and eventually will break into smaller ones, leaving behind a very dense bubble plume that will be visible in the next step of the analysis.

3.2 Bubble characteristics

The bubble plume under a falling jet is an interesting phenomena to observe. It is a case of multiphase flow where many parameters can be considered especially when the number and sizes of the bubbles are also dependant on the velocity of the falling jet. These bubbles are not only tracers of the present flow but also a consequence of it. However reliable measurements of this plume become difficult when the density of bubbles and range of sizes is high. In this section we present the results of an attempt to extract information from different plume conditions and the advantages and limitations of the 3D PTV technique used to perform the analysis.

In Figure 6(a) the index p, presented in equation 3, is shown for all different analyzed cases. Although in all cases $p > 1$, it is only in a few cases where $p > 5$, the value for which mislinks reduce considerably according to Malik et al. (1993). This means that the bubbles can be tracked but with certain difficulty.

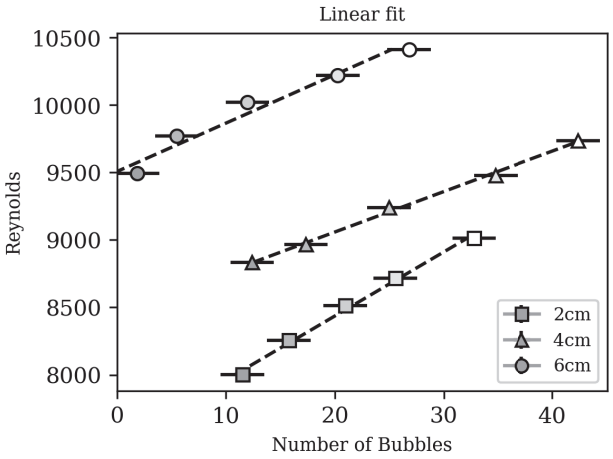

Figure 5: Reynolds of the falling jet against number of bubbles. The graph shows the estimated Reynolds number of the falling jet when impinging in the pool and compares it with the mean number of bubbles visible in the image sequence. It is visible that the amount of bubbles is directly proportional to the Reynolds number. The fitted lines are $0.028(05)x - 265(5)$ for d=2 cm, $0.021(05)x - 157(5)$ for d=4 cm, $0.033(05)x - 282(5)$ for d=6 cm.

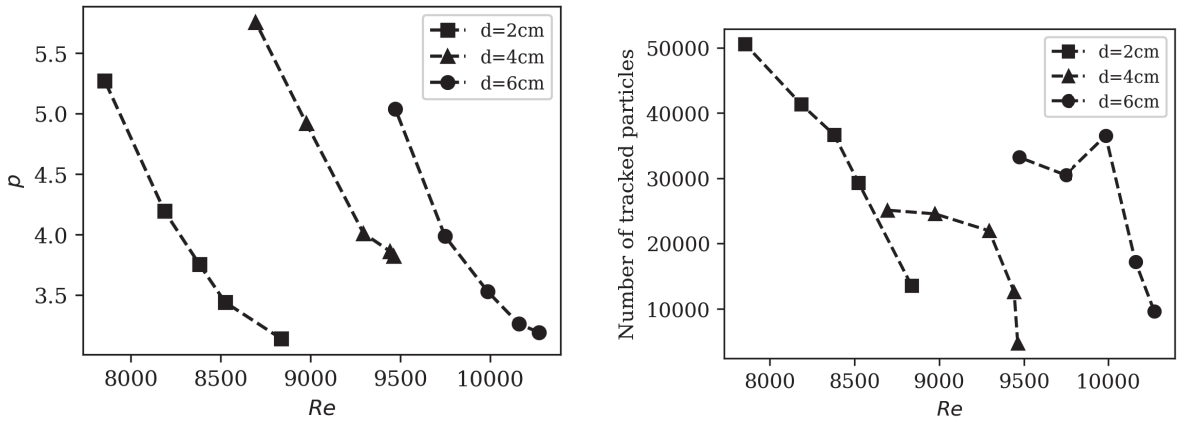

(a) Different values of p for all the cases analyzed in this study. We compare with the velocity of the jet in the impingement point and we see the difference for the falling distances.

(b) Total number of particles tracked in at least two consecutive frames compares with the Reynolds number of the jet.

Figure 6: Graph of different values of p and total particles tracked in at least two consecutive frames

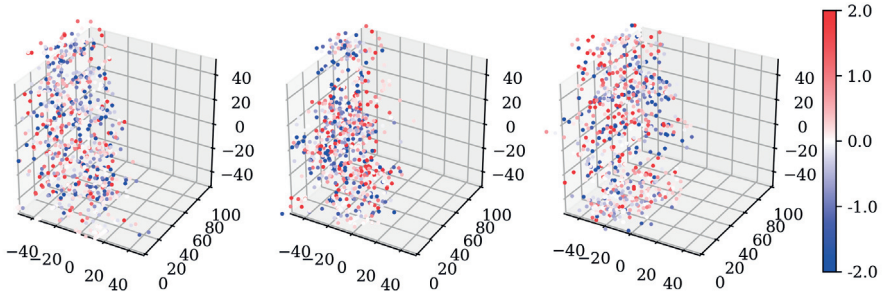

(a) Bubbles 3D positions. The colour represents the instant velocity in the vertical direction, red points indicate bubbles moving downwards and blue points indicate bubbles moving upwards.

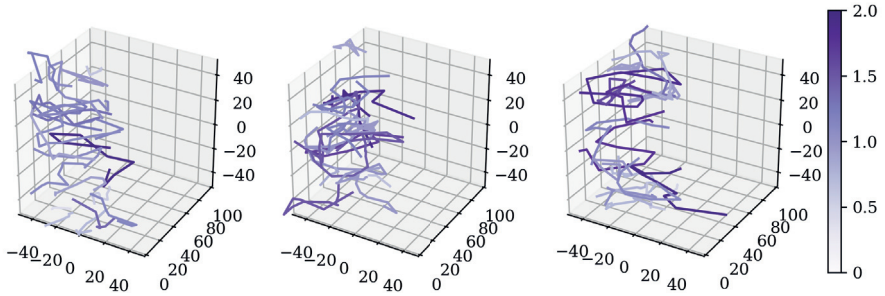

(b) Bubbles 3D trajectories. The colour of the plot indicates the magnitude of the velocity vector. The darker the colour, the faster the bubble moves.

Figure 7: Results of 3DPTV tracking

Therefore, it is important to use carefully the parameters needed to track the particles during the procedure. In Figure 6(b), the efficiency of the tracking algorithm is shown. For this type of dense plume, the amount of particles that can be traced to the next step decreases with increasing Reynolds. Surprisingly, the amount of bubbles that can be followed for more than 10 times steps seems to increase with the Reynolds number, as it is shown in Table 2.

The trajectories of the bubbles and their velocities can be found in Figure 7 . From left to right results for the different falling distances d are presented. No distinguishable difference can be seen in the velocity fields shown in Figure 7(a). For all the cases there are bubbles moving upwards and downwards with considerable high velocity. Perhaps a separation of the bubble velocities depending on the bubble size could give a certain trend for the different d and Re. From Figure 7(b) it is possible to observe that the movement of the bubbles is also great in the horizontal plane. This is expected as the common trajectories for the bubbles are helicoidal, specially when the bubbles have considerable big diameter. This behaviour is probably enhanced by the jet velocity. It is important to mention that the total length of the bubbles plume is not visible in the analysis therefore no conclusion can be obtained on the length of the plume from this analysis.

In Figure 8 some probability distributions are shown for the higher Re in each distance. In Figure 8(a) the distribution of the bubbles around the center of the jet is shown while Figure 8(b) shows the distribution of vertical velocities. Bubbles that move downwards have negative velocity while bubbles that move upwards have positive velocity. In Figure 8(c) typical size distribution are presented. No remarkable differences are visible in the distributions.

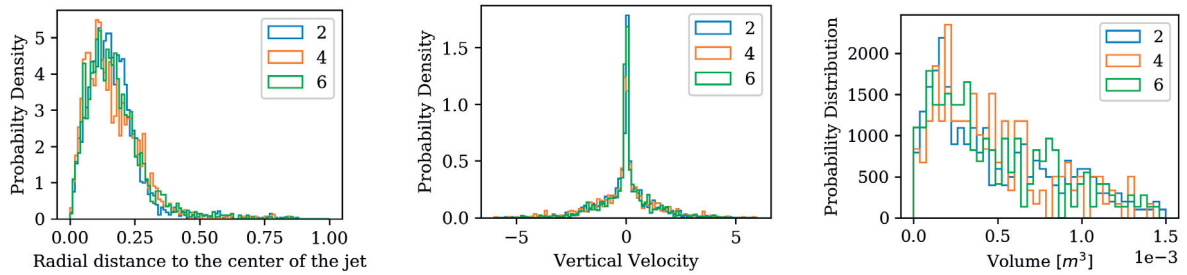

(a) Position to the center of the jet. The x axis represents the distance r/l where r is the distance of the bubble to center and l is the total FOV length.

(b) Vertical velocities of the bubbles in the plume for different falling distance.

(c) Size Distribution of Bubbles in the plume for different falling distance.

Figure 8: Different Distributions

d = 0.02 m	*Re*	7854	8186	8381	8524	8837
	%	5	7	6	6	11
d = 0.04 m	*Re*	8694	8975	9294	9441	9462
	%	5	6	6	8	27
d = 0.06 m	*Re*	9471	9747	9985	10159	10269
	%	5	6	1	11	10

Table 2: Comparison of the Reynolds number with the percentage of particles that are tracked for at least 10 frames. The data from the different jet lengths d is shown.

4 Conclusions

In this work a bubble plume created by a circular free falling jet was studied by means of imaging techniques. From image sequences of the air entrainment process qualitative relations between the jet characteristics and the bubbles created were found. Further, a linear trend was obtained when comparing the Reynolds number and the bubble count. The trajectories of the bubbles were reconstructed, in spite of the variability of the sizes.

The results presented are promising for further analysis. In the future we aim to improve the tracking by addressing in a robust manner the case of bubble break up into two or more bubbles. Such tools could then be applied to study dynamics of the jet after the impact, in particular, for reliable reconstruction of bubble trajectories.

Acknowledgements

This project is a part of a RCN funded project; Petromaks2/ 256435, RigSpray. The authors wish to acknowledge the OpenPTV project and Alex Liberzon for their support while using the OpenPTv software. Laboratory Head Engineer Olav Gundersen is also acknowledged for the assistance he provided for the experimental work.

References

Bodaghkhani A, Dehghani SR, Muzychka YS, and Colbourne B (2016) Understanding spray cloud formation by wave impact on marine objects. *Cold Regions Science and Technology* 129:114–136

Borisenkov YP and Pchelko I (1975) Indicators for forecasting ship icing. Technical report

Chanson H, Aoki S, and Hoque A (2006) Bubble entrainment and dispersion in plunging jet flows: fresh-water vs. seawater. *Journal of Coastal Research* pages 664–677

Chanson H, Aoki Si, and Hoque A (2004) Physical modelling and similitude of air bubble entrainment at vertical circular plunging jets. *Chemical engineering science* 59:747–758

Deane GB (1997) Sound generation and air entrainment by breaking waves in the surf zone. *The journal of the acoustical society of America* 102:2671–2689

Dommermuth DG, O'Shea TT, Wyatt DC, Ratcliffe T, Weymouth GD, Hendrikson KL, Yue DK, Sussman M, Adams P, and Valenciano M (2007) An application of cartesian-grid and volume-of-fluid methods to numerical ship hydrodynamics. Technical report. SCIENCE APPLICATIONS INTERNATIONAL CORP SAN DIEGO CA

Kiger KT and Duncan JH (2012) Air-entrainment mechanisms in plunging jets and breaking waves. *Annual Review of Fluid Mechanics* 44:563–596

Kolaini AR (1998) Sound radiation by various types of laboratory breaking waves in fresh and salt water. *The Journal of the Acoustical Society of America* 103:300–308

Legendre D, Zenit R, and Velez-Cordero JR (2012) On the deformation of gas bubbles in liquids. *Physics of Fluids* 24:043303

Maas H, Gruen A, and Papantoniou D (1993) Particle tracking velocimetry in three-dimensional flows. *Experiments in fluids* 15:133–146

Malik N, Dracos T, and Papantoniou D (1993) Particle tracking velocimetry in three-dimensional flows. *Experiments in Fluids* 15:279–294

Ryerson CC (2013) Icing management for coast guard assets. Technical report. ENGINEER RESEARCH AND DEVELOPMENT CENTER HANOVER NH COLD REGIONS RESEARCH

Soh WK, Khoo BC, and Yuen WD (2005) The entrainment of air by water jet impinging on a free surface. *Experiments in fluids* 39:498–506

Wang H, Bertola N, and Chanson H (2016) Bubble entrainment in vertical plunging jets

Willneff J (2003) *A spatio-temporal matching algorithm for 3D particle tracking velocimetry*. Ph.D. thesis. ETH Zurich

Zhu Y, OĞUZ HN, and Prosperetti A (2000) On the mechanism of air entrainment by liquid jets at a free surface. *Journal of Fluid Mechanics* 404:151–177